A&A, 713, A202 (2026)
https://doi.org/10.1051/0004-6361/202660699
© The Authors 2026

Astronomy & Astrophysics

The type Ia supernova 2023vjh: A peculiar 1991bg-like supernova with unusually faint light curves

M. Kopsacheili[1,2,⋆], L. Galbany[1,2], G. Folatelli[3,4], M. M. Phillips[5], C. R. Burns[6], M. D. Stritzinger[7], H.-Y. Miao[1,2], M. González-Bañuelos[1,2], R. García-Benito[8], T. E. Müller-Bravo[9,10], E. Y. Hsiao[11], K. Auchettl[12,13], J. P. Anderson[14], C. Ashall[15], T.-W. Chen[16], D. D. Desai[15], M. E. Huber[15], T. de Jaeger[17], J. M. DerKacy[18], M. Gromadzki[19], J. T. Hinkle[20,21,15], W. Hoogendam[15], C. Jimenez-Palau[1,2], K. Matilainen[22], P. A. Mazzali[23,24], K. Medler[15], N. Morrell[25], T. Pessi[14], C. Pfeffer[15], K. Phan[1,2], G. Pignata[26], A. Polin[27], R. Sanfeliu[1,2], B. J. Shappee[15], M. A. Tucker[28], H. Xiao[11], and D. R. Young[29]

(Affiliations can be found after the references)

Received 29 April 2026 / Accepted 8 July 2026

ABSTRACT

We present observations of the 1991bg-like type Ia supernova (SN Ia) 2023vjh associated with the elliptical galaxy MCG+04-10-013. Its light-curve shape parameters ($\Delta m_{15}(B) = 1.89 \pm 0.01$ mag and $s_{BV} = 0.45 \pm 0.03$) together with its spectroscopic evolution place it firmly within the class of fast-declining subluminous SNe Ia. The near-peak spectra show prominent features of Si II, Ca II, and Ti II consistent with a cool photosphere and place SN 2023vjh within the 'cool' and extremely cool regions on the classification diagrams. In addition, the three late-phase near-infrared (NIR) spectra display the Ca II NIR triplet, Fe II, and Co II absorptions but no obvious H-band break. Although SN 2023vjh falls in the same regions of the classification diagrams as other well-studied 91bg-like events, it shows some deviation within this class. In particular, it is systematically fainter than predicted by explosion models and fainter than other well-studied 91bg-like SNe. Light-curve fitting and colour-based analyses indicate a relatively large reddening ($E(B-V)_{host} \sim 0.2$–0.35 mag), which is unusual for 91bg-like SNe. Yet the lack of detectable Na I D absorption in its spectra, along with its large projected distance from the centre of its passive host galaxy (6.8 kpc), suggests that interstellar extinction along the line of sight is minimal. SN 2023vjh appears to be fainter than typical 91bg-like SNe, and it could be affected by circumstellar material (CSM). Comparisons with explosion models and alternative extinction prescriptions show that including CSM-like extinction improves agreement in the blue bands, but residual discrepancies in the i-band may reflect limitations in the model.

Key words. supernovae: general – supernovae: individual: SN 2023vjh – supernovae: individual: 91bg-like SNe Ia

1. Introduction

Supernovae are of crucial importance for the interstellar medium (ISM), as they enrich it with heavy elements (Raiteri et al. 1996) and deposit large amounts of energy into it. More specifically, type Ia supernovae (SNe Ia) produce the majority of iron-group elements in the Universe (Hamuy et al. 2003). They are also standardizable candles (Phillips 1993), and they enable precise measurements of cosmological parameters such as the Hubble constant (Riess et al. 1998; Perlmutter et al. 1999).

For normal SNe Ia, there is a tight relationship between peak luminosity and their light-curve decline rate relation, and it is commonly parametrised by $\Delta m_{15}(B)$, the decline in B-band magnitude during the first 15 days after maximum light (Pskovskii 1977; Phillips 1993), or by the colour-stretch parameter s_{BV}, which describes the time evolution of the $B-V$ colour curve – defined as $s_{BV} = t_{max}(B-V)/30$, where $t_{max}(B-V)$ is the maximum of the $B-V$ colour curve, measured relative to the epoch of the B-band maximum (Burns et al. 2014) – as well as the colour at peak (Riess et al. 1996; Tripp 1998). These relations make SNe Ia very useful for cosmological distance measurements. Their use led to the unexpected discovery of the accelerated expansion of the Universe and the recognition of dark energy as the dominant component driving it today (Riess et al. 1998; Perlmutter et al. 1999). Today, SNe Ia continue to provide precise measurements of the expansion rate of the Universe, with the most recent determination of the Hubble constant from normal SNe Ia: $H_0 = 73.18 \pm 0.88\,\mathrm{km\,s^{-1}\,Mpc^{-1}}$ (Riess et al. 2025).

Type Ia SNe are found in all types of galaxies, even in non-star-forming galaxies, indicating that the progenitors are most probably compact stars. The broad homogeneity of observed properties among SNe Ia suggests a common progenitor system. Although they are widely believed to originate from the thermonuclear explosion of a carbon-oxygen (C-O) white dwarf (WD) in a close binary system (Hoyle & Fowler 1960), the specific nature of the progenitor systems and explosion mechanisms remain under debate. Two main scenarios are often considered: the single-degenerate (SD) channel, involving a C-O WD accreting matter from a non-degenerate companion, such as a main-sequence or red giant star (Whelan & Iben 1973; Livne 1990), and the double-degenerate (DD) channel, which consists of two C-O WDs (e.g. Nomoto 1980). Observational evidence exists for both. For instance, the absence of a surviving companion in some remnants supports DD origins (Tucker et al. 2020), whereas events such as SN 2012Z, potentially linked to a helium-rich donor (McCully et al. 2022; Stritzinger et al. 2015; McCully et al. 2014), and SN 2002ic, associated with a massive asymptotic giant branch star (Hamuy et al. 2003), favour SD systems. Among these progenitor scenarios,

⋆ Corresponding author: kopsacheili@ice.csic.es (MK)

Open Access article, published by EDP Sciences, under the terms of the Creative Commons Attribution License (https://creativecommons.org/licenses/by/4.0), which permits unrestricted use, distribution, and reproduction in any medium, provided the original work is properly cited.
This article is published in open access under the Subscribe to Open model. Subscribe to A&A to support open access publication.

four explosion mechanisms are commonly discussed: (a) violent mergers of two C–O WDs, where the explosion is triggered during the merging process (García-Berro & Lorén-Aguilar 2017); (b) Chandrasekhar-mass explosions, where a WD close to the Chandrasekhar limit ignites centrally due to compressional heating from accretion from the donor star, possibly a red giant, a low-mass (<7–8 $M\odot$) main-sequence star, an He star, or a tidally disrupted WD in a DD system (Hoyle & Fowler 1960; Whelan & Iben 1973; Nomoto 1982; Piersanti et al. 2004); (c) sub-Chandrasekhar explosions via the double-detonation mechanism, involving a helium shell detonation that ignites the C–O core (Nomoto 1980; Livne 1990; Woosley & Weaver 1994; Hoeflich & Khokhlov 1996; Hoeflich et al. 2017; Kromer et al. 2010; Maeda et al. 2018; Polin et al. 2019); (d) mergers with masses below, equal to, or above the Chandrasekhar mass (Iben & Tutukov 1984; Webbink 1984; Pakmor et al. 2010, 2013; Scalzo et al. 2010; van Kerkwijk et al. 2010; Kromer et al. 2013, 2016) in triple or quadruple systems, where dynamical interactions induce high-eccentricity orbits that lead to a head-on impact (Thompson 2011; Pejcha et al. 2013; Shappee & Thompson 2013).

Apart from the normal SNe Ia, there are various subtypes that present different photometric and/or spectroscopic characteristics from the normal SNe Ia, suggesting different explosion mechanisms. One of them is the sub-luminous sub-class of 91bg-like SNe. The prototype of this peculiar class, SN 1991bg, was extensively studied by Filippenko et al. (1992); Leibundgut et al. (1993) and Turatto et al. (1996) Since then, more than 160 91bg-like SNe have been discovered; see, for example, the Transient Name Server (TNS[1]) and the Carnegie Supernova Project (CSP; Hamuy et al. 2006; Contreras et al. 2010; Krisciunas et al. 2017, Hoogendam et al. 2022; Pearson et al. 2024; Alburai et al. 2026).

Similar to normal SNe Ia, the spectra of 91bg-like SNe show no evidence of H or He, but they do exhibit strong absorption from Si II (Filippenko 1997). Around peak brightness, they also show absorption features from several intermediate-mass elements, including Si, Mg, Ca, S, and O, which is consistent with their classification as thermonuclear explosions (Filippenko 1997).

However, 91bg-like SNe present strong O I λ 7774 and Ti II lines between 4000 and 4400 Å in the early spectra (e.g. Taubenberger 2017; Galbany et al. 2019). They are characterised by relatively low ejecta velocities, although not dramatically lower than those in normal SNe Ia, with no high-velocity features (HVFs) observed up to now (unlike many SN Ia; Mazzali et al. 2005). It remains uncertain whether the lack of HVFs in 91bg-like SNe is driven by their explosion physics or by the nature of their surrounding environment (Taubenberger 2017).

In addition, 91bg-like events usually show notable differences in their light curves compared to standard SNe Ia, suggesting a different explosion mechanism or progenitor system. Photometrically, 91bg-like SNe are fainter at their peak, and they rise and decline faster than normal SNe Ia, placing them at the lower-right part (i.e. faint and fast-evolving part) of the width-luminosity relation. The light curve in the near-infrared (NIR) bands lacks the secondary maxima typical of normal SNe Ia, and hence they present a single peak that occurs a few days later than in the B band (e.g. Garnavich et al. 2004), while in normal SNe Ia, the NIR maxima happens approximately 3 days before the B_{max} (e.g. Krisciunas et al. 2004a).

The luminosity-width relation of SNe Ia is assumed to be mainly driven by the amount of ^{56}Ni synthesised during the explosion (Arnett 1980). Less luminous SNe are expected to eject smaller amounts of ^{56}Ni, typically less than 0.1 $M_\odot$ in the case of 91bg-like SNe (Stritzinger et al. 2006); however, the light curve might be affected by the total amount of ejected mass. Pakmor et al. (2013) suggest a binary system of He and C-O WDs as the probable progenitor scenario of 91bg-like SNe since small ejecta mass could explain the narrow light curves.

Most 91bg-like SNe are found in elliptical galaxies, which are dominated by old stellar populations and lack ongoing star formation (Taubenberger 2017; Dimitriadis et al. 2025). This host galaxy preference supports the idea of older progenitor systems. Only a few 91bg-like SNe have been found in spiral galaxies, for example, SN 1999by, which occurred in the spiral galaxy NGC 2841 (Höflich et al. 2002; Garnavich et al. 2004), and SN 2022xkq, found in the barred-spiral galaxy NGC 1784 (Pearson et al. 2024). Within the Lick Observatory Supernova Search sample (Li et al. 2011), 91bg-like events make up approximately 18% of all SNe Ia (or more than 6.7% according to Desai et al. (2024, 2026)).

Low-luminosity fast-declining SN Ia, such as the 91bg-like sub-class, are often excluded from cosmological analyses because their photometric and spectroscopic properties deviate from those of normal SNe Ia and they do not follow the standard light-curve width–luminosity relation used to standardise SN Ia distances. In particular, their rapid decline rates and intrinsically red colours make them difficult to model with commonly used light-curve fitters, and cosmological samples often remove fast decliners (e.g. objects with s_{BV} <0.5). Nevertheless, several studies have suggested that these events can still be standardised when appropriate parameters are used. Using the colour-stretch parameter s_{BV}, Burns et al. (2014, 2018) showed that fast-declining SNe Ia follow a continuous luminosity–decline relation extending from normal to subluminous objects. Hoogendam et al. (2022) compared the distance moduli of the subluminous SN 2015bo and SN 1997cn with those derived from surface brightness fluctuations (Jensen et al. 2021) and from z_{cmb}-corrected cosmology. They found good agreement and suggested that fast decliners could be as standardizable as normal SNe Ia. More recently, Graur (2024) and Phillips et al. (2026) revisited the suitability of these objects as distance indicators. In particular, Phillips et al. (2026) analysed a Hubble-flow sample of fast-declining SNe Ia from CSP and demonstrated that distances derived using the Tripp method (Tripp 1998), where the peak luminosity is modelled as a function of light-curve shape and colour, yield values of the Hubble constant consistent with those obtained from normal SNe Ia. They also introduced a simplified 'colour method' based solely on the observed ($B_{max} - V_{max}$) pseudo-colour at maximum light, which does not require light-curve shape information. Remarkably, this approach provides comparable distance estimates and reflects the strong dependence of peak luminosity on photospheric temperature in fast-declining SNe Ia, rather than being driven purely by dust reddening. These results suggest that despite often being excluded from cosmological samples, 91bg-like SNe Ia may still serve as useful distance indicators when treated with appropriate standardisation methods.

In this paper, we present photometric and spectroscopic observations of SN 2023vjh, a subluminous 91bg-like SN Ia that occurred in the elliptical galaxy MCG+04-10-013. Its photometric and spectral properties are consistent with those of other well-studied 91bg-like events. However, SN 2023vjh appears to be a special case within this sub-class, as its dimness and inferred reddening are unusually high compared to typical 91bg-like SNe,

[1] https://www.wis-tns.org/

Table 1. Main properties of the SN 2023vjh and its host galaxy MCG+04-10-013.

Parameters	Values	Ref
SN 2023vjh		
RA, Dec (J2000)	04:02:39.2, +25:14:00.5	(1)
	60.663250, 25.233533	(1)
Explosion date (MJD)	60 234.2 ± 0.4	This work
T_{max}(B) (MJD)	60245.8 ± 0.4	This work
$E(B-V)_{MW}$	0.236 ± 0.008	(2)
Δm_{15}(B)(mag)	1.89 ± 0.01	This work
S_{BV}	0.45 ± 0.03	This work
Host galaxy		
Name	MCG+04-10-013	(4)
Type	−2.7 D	(5)
RA, Dec (J2000)	04:02:37.9, +25:13:58.3	(4)
Redshift	0.0192 ± 0.000037	(6)
Distance (Mpc)	83.2± 5.8	(6), (7)
M_B	20.13 ± 0.53	(8)

Notes. (1) ATLAS survey (Tonry et al. 2018b); (2) Schlafly & Finkbeiner (2011); (3)Schlegel et al. (1998); (4) Simbad; (5) Kochanek et al. (2001); (6) Lavaux & Hudson (2011); (7) Fixsen et al. (1996); (8) Paturel et al. (2003).

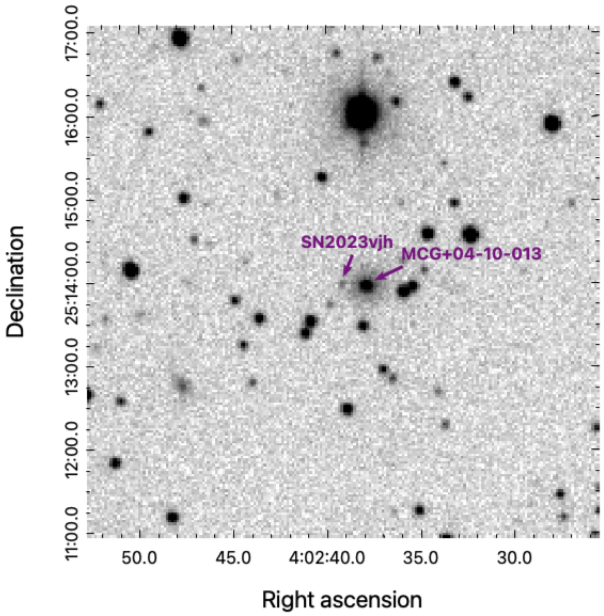


Fig. 1. Field of the SN 2023vjh and its host galaxy MCG+04-10-013. The image is taken from the ATLAS RC2 survey (m17 field), retrieved through the DS9 data server interface.

despite the lack of clear spectroscopic evidence of significant host-galaxy extinction. The paper is organised as follows: the observations and the data reduction are described in Sect. 2. Information on the host galaxy and its properties is presented in Sect. 3. In Sects. 4 and 5 we further investigate the possible host-galaxy extinction through a series of tests, exploring different empirical and model-based approaches to assess whether the observed faintness and colours can be explained by dust or whether intrinsic effects are required while also discussing the photometric and spectroscopic properties and their calculation methods. Finally, in Sect. 6, we summarise our results.

2. SN 2023vjh observations and reduction

The supernova 2023vjh was discovered on 17 October 2023 (MJD = 60 234.342) by ZTF with a magnitude of 21.18 in the g-ZTF band, and it was subsequently classified as a SN Ia 1991bg-like at z = 0.019 (by the Spectroscopic Classification of Astrophysical Transients group - SCAT; Tucker et al. 2022). It is possibly associated with the galaxy MCG+04-10-013, an elliptical galaxy at a redshift distance of 83.2 ± 5.8 Mpc, calculated from the galaxy's CMB-frame velocity (5642±8 km s^{-1}; Fixsen et al. 1996), a redshift of 0.019 ± 1.2×10^{-5} (Lavaux & Hudson 2011), and assuming H_0 = 67.8 ± 4.7 km s^{-1} Mpc^{-1} (Planck Collaboration XIII 2016). The explosion took place 6.8 kpc (projected distance) from the galaxy centre (see Fig. 1). The main properties of SN 2023vjh and its host galaxy are presented in Table 1. The photometry sequence and the spectroscopic log are presented in Appendix A

2.1. Photometry

The object SN 2023vjh was observed as part of the Precision Observations of Infant Supernova Explosions (POISE) program (Burns et al. 2021). POISE uses the Henrietta Swope 1 m telescope at Las Campanas Observatory to confirm SN candidates and follow infant SN explosions from public transient survey streams such as the Zwicky Transient Facility (ZTF; Bellm et al. 2019) and the Asteroid Terrestrial-impact Last Alert System (ATLAS; Tonry et al. 2018b), complemented by spectroscopic observations from multiple facilities.

The POISE follow-up of SN 2023vjh began shortly after discovery and extended over approximately two months. Optical imaging was obtained in the B, V, g, r, i, u filters and processed using the POISE photometric pipeline, which closely follows the procedures of CSP (Contreras et al. 2010; Krisciunas et al. 2017). Briefly, the raw frames are bias- and flat-field corrected using nightly calibration data, and astrometric solutions are derived using the Refcat2 standard star catalogue (Tonry et al. 2018a).

Because POISE is a follow-up program rather than a discovery survey, it does not routinely obtain template images for host-galaxy subtraction. Instead, archival imaging from Pan-STARRS (Kaiser et al. 2002) or SkyMapper (Wolf et al. 2018) is used when required.

Photometric calibration is performed by transforming Refcat2 magnitudes of local field stars into the CSP natural $BVgri$ system. The transformation relations were derived from long-term CSP local sequence calibrations and are described in Krisciunas et al. (2017) and Phillips et al. (2019).

We also include forced-photometry light curves from ZTF (g, r; difference-imaging photometry) and ATLAS (c, o; Shingles et al. 2021). Detections are defined as observations with a signal-to-noise ratio >3. The observed magnitudes are presented in Tables A.1 and A.2 for POISE and ZTF/ATLAS, respectively.

For the extinction correction, we adopted the reddening law of Cardelli et al. (1989), taking into account the MW extinction. The MW component was estimated using $E(B-V)$ = 0.236 ± 0.008 mag from Schlegel et al. (1998); Schlafly & Finkbeiner (2011), assuming R_V = 3.1.

2.2. Spectroscopy

2.2.1. Optical spectra

The spectra of SN 2023vjh have been obtained with the following telescopes/instruments: University of Hawaii 2.2 m telescope (UH88), its Supernova Integrated Field Spectrograph (SNIFS; Lantz et al. 2004; Tucker et al. 2022) instrument, the 10.4 m Gran Telescopio CANARIAS (GTC), its Optical System for Imaging and low-resolution Spectroscopy OSIRIS[2] (grisms R1000B and R1000R), the Keck Cosmic Web Imager (KCWI) of the 10 m Keck II telescope in Hawaii Martin et al. (2010), the Andalusia Faint Object Spectrograph and Camera (ALFOSC) of the 2.56 m Nordic Optical Telescope (NOT; Djupvik & Andersen 2010), the 2.0 m Liverpool Telescope (LT; Steele et al. 2004) using the Spectrograph for the Rapid Acquisition of Transients (SPRAT; Piascik et al. 2014), the New 3.58 m Technology Telescope (NTT) obtained by the PESSTO collaboration (Smartt et al. 2015) using the ESO Faint Object Spectrograph and Camera (EFOSC2; Buzzoni et al. 1984), the Inamori-Magellan Areal Camera and Spectrograph (IMACS) of the Magellan Baade Telescope at Chile's Las Campanas Observatory Dressler et al. (2011), and the PPAK mode of the Potsdam Multi Aperture Spectrograph (PMAS; (Verheijen et al. 2004; Kelz et al. 2006)) of the 3.5 m telescope of the Centro Astronómico Hispano Alemán (CAHA).

Before any kind of analysis, we applied some corrections to the spectra. First, we followed a procedure known as 'colour matching', according to which they are scaled to match the photometry (Hsiao et al. 2007). Then we applied the MW extinction correction, and finally we corrected from observed flux to rest-frame flux.

The spectral uncertainties were estimated using a Savitzky–Golay filtering technique. Each spectrum was smoothed with a polynomial fit using window sizes between 41 and 101 resolution elements, chosen to trace the overall continuum while suppressing small-scale features. The difference between the original and smoothed spectra provided residuals that reflect the local noise. The wavelength-dependent root mean square (RMS) of these residuals was adopted as the uncertainty, $\sigma(\lambda)$, which typically increases towards the blue, noisier regions of the spectra. The bluest and reddest portions with flux/$\sigma(\lambda)$ below three were excluded from the visual presentation. The log of the spectroscopic observations is listed in Table A.4

2.2.2. NIR spectra

Near-infrared spectra were obtained at epochs +16.4, +20.8, and +23.4 days with respect to the epoch of B band maximum. Those at +16.4 and +23.4 days were taken with the Folded-port InfraRed Echellette (FIRE) spectrograph installed on the Baade Telescope. The data were processed with the IDL *fire-hose* pipeline (Simcoe et al. 2013), which is specifically built for reducing FIRE observations. The pipeline carries out flat-field correction, wavelength calibration, sky subtraction, spectral tracing, and spectral extraction. More detailed description of the reduction can be found in Hsiao et al. (2019).

The spectrum at epoch +20.8 days was obtained with the Espectrógrafo Multiobjeto Infra-Rojo (EMIR; Garzón et al. 2022) mounted on the GTC. Sixteen 120 s exposures were taken using the YJ and HK gratings. The data were reduced with a custom pipeline that performs the standard calibrations, removes telluric absorption using observations of a telluric standard obtained immediately after the SN, and applies the flux calibration. The spectra were corrected for Milky Way extinction, in the same manner as the optical spectra.

[2] https://www.gtc.iac.es/instruments/osiris/

3. The host galaxy of SN 2023vjh

Integral field spectroscopy (IFS) of the host galaxy MCG+04-10-013 was obtained on 16 December 2023, with the PMAS (Roth et al. 2005) in PPak mode of the 3.5 m telescope of the Centro Astronómico Hispano Alemán (CAHA) at Calar Alto Observatory, as part of the PMAS/PPak Integral-field Supernova hosts COmpilation (PISCO; Galbany et al. 2018). The PPak instrument is a hexagonal bundle, and it consists of 331 fibres of 2.7 arcsec each (spatial sampling). The field of view of the bundle is ∼1.3 arcmin^2. We acquired three exposures of 900 s each and with small positional shifts between them. The observations were performed with the V500 grating that covers the range of 3750–7500 Å, with a spectral resolution of 6 Å.

The optical spectroscopic data of MCG+04-10-013 were reduced using a customised version of the CAVITY data reduction pipeline (García-Benito et al. 2024), adapted to the specific requirements of this study. The general workflow follows the standard CAVITY procedure, including CCD frame combination and cleaning, spectral extraction, wavelength and flux calibration, sky subtraction, and final cube reconstruction. The reduction process accounts for Poisson and readout noise propagation, cosmic-ray removal (via PyCosmic; Husemann et al. 2012), and bias and gain correction for the multi-amplifier CCD configuration used in the PPAK/PMAS instrument. Calibration frames taken within 1.5 h of the science exposures were used to mitigate flexure effects, with wavelength solutions refined using sky lines to ensure subpixel accuracy. Stray light was modelled and subtracted prior to optimal spectral extraction (Horne 1986). The extracted spectra were resampled to a common linear wavelength grid, and fibre-to-fibre transmission differences were corrected using twilight flats.

Flux calibration was performed using a sensitivity curve derived from spectrophotometric standard stars observed with the same instrument setup. Atmospheric extinction corrections were applied using airmass-dependent coefficients monitored by the Calar Alto Visual Extinction (CAVEX) system. The initial Galactic extinction correction applied during the PMAS data reduction used the reddening maps of Schlegel et al. (1998) together with the extinction law of Cardelli et al. (1989). However, throughout the remainder of this work, Milky Way reddening corrections are based on Schlafly & Finkbeiner (2011). Therefore, after extracting the supernova spectrum from the PMAS data, we re-applied the Galactic extinction correction using the Schlafly & Finkbeiner (2011) reddening value, which corresponds to 0.86 times the $E(B-V)$ from Schlegel et al. (1998). As a result, all spectra and photometric measurements presented in this work were corrected consistently using the Schlafly & Finkbeiner (2011) extinction estimate. Sky subtraction employed the median of the 30 faintest of the 36 dedicated PPak sky fibres to avoid contamination from field sources.

The final data cube was reconstructed using an inverse-distance weighting interpolation scheme (Sánchez et al. 2012) with a Gaussian kernel of $\sigma = 0.75''$, yielding a spatial sampling of $1.0''$. Differential atmospheric refraction was corrected iteratively.

We used the IFS data of the galaxy to estimate its age and the stellar metallicity. The first step was to extract the spectrum of the galaxy. To do so, we started by masking out the position

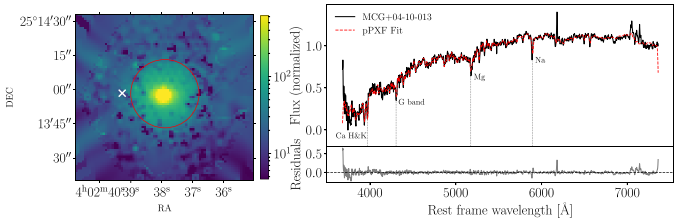


Fig. 2. *Left*: collapsed 2D image of the galaxy, obtained by summing the flux over all wavelengths (from a PMAS cube at CAHA). The red circle marks the radius containing 90% of the galaxy light, and the white 'X' indicates the masked position of SN 2023vjh. *Right*: spectrum of the galaxy extracted within the same radius (black line) with the best-fit model from pPXF overplotted (red line). The residuals of the fit are shown in grey in the lower panel.

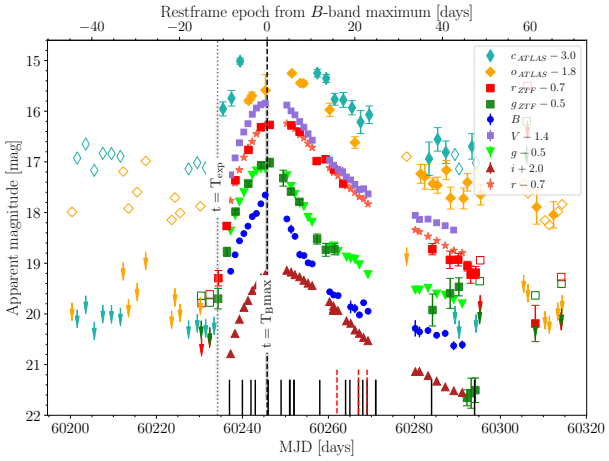


Fig. 3. Optical light curves of SN 2023vjh. The grey dotted line represents the explosion date (see Fig. A.1), and the black dashed line shows the epoch of brightness in the B band obtained from a `SNooPy` fit (see Fig. A.2). The black lines at the bottom represent epochs with optical spectra available, while the red dashed lines show those with NIR spectra available.

of the supernova and replacing the NaN values with interpolated fluxes from the surrounding pixels. In order to define the aperture to extract the spectrum of the galaxy, we collapsed the cube into a 2-dimensional image summing over the spectra, constructed the curve of growth and selected the aperture that contains the 90% of the total flux (red circle on the left panel of Fig. 2)

The spectrum of MCG+04-10-013 is shown on the right panel of Fig. 2 (black line). It is a typical spectrum of an elliptical galaxy characterised by strong absorption lines due to metals and molecules in the stellar atmospheres. Some of those (Ca H&K, CH G band, Mg b triplet, Na D doublet) are also indicated in the spectrum.

For the estimation of the stellar age and metallicity we employed the publicly available penalised pixel-fitting (pPXF) code (Cappellari & Emsellem 2004; Cappellari 2023) to model the observed spectra as linear combinations of simple stellar populations (SSPs) drawn from the MILES stellar library (Vazdekis et al. 2010; Cenarro et al. 2007; Sánchez-Blázquez et al. 2006). The MILES library spans a spectral range of 3525–7500 Å, with stellar metallicities covering [M/H] from +0.22 to −2.3, and ages ranging approximately from 0.06 to 18 Gyr. We explored two forms of the initial mass function (IMF): the unimodal (UN) and the bimodal (BI) modes. The unimodal IMF is a single power-law characterised by a logarithmic slope (Γ), for which thirteen values ranging from 0.3 to 3.5 are considered. The bimodal IMF shares the same set of slope values, denoted Γ_b, but differs in shape: It behaves similarly to the unimodal IMF for stellar masses above 0.6 $M_\odot$, while the slope flattens at lower masses, reducing the contribution from low-mass stars through a smooth transition to a shallower profile. The UN mode provided a slightly better fit, and therefore we present the results obtained using this IMF. The output gives the weighted average age and metallicity of the stellar population, with the weights reflecting the relative contributions of each SSP sampled across a regular grid in log(age) and metallicity. The best-fit spectrum, shown in red in Fig. 2, corresponds to a stellar population with an age of 12.16 Gyr, a metallicity of [M/H] = −0.10, and an IMF slope of 0.99 (in this parametrisation, a Kroupa/Chabrier-like IMF corresponds to Γ = 1.30; Kroupa 2001; Chabrier 2003). Those values are common in elliptical galaxies that host 91bg-like SNe (e.g. Fig. 3 in Panther et al. 2019).

4. Photometric properties

4.1. Light curves

The light curves Swope$-BVgri, ZTF-gr$, and *ATLAS-co* of SN 2023vjh are presented in Fig. 3. The light curves show a single peak in all bands, with nearly daily coverage from about 11 days before maximum to roughly one month after. We first calculated the explosion time with the most straightforward method, which is the mean value between the last non-detection and the first detection in the *ZTF-g* band, and we found t_0 = 60 233.4 ± 1.0 MJD. Then, following a similar approach to Galbany et al. (2025), we performed a simultaneous fit to the early rise of the g, r, $ZTF-g$, and $ZTF-r$ light curves using a power-law model. The fit included observations from the last two non-detections up to the epoch at which the flux reached half of its maximum value in the red and green bands (POISE and ZTF). All bands were fitted jointly, adopting a single explosion epoch, t_0, common to all light curves while allowing the remaining power-law parameters (e.g. normalisation and rise index) to vary independently for each band. For each band, the flux evolution was modelled as

$$f(t) = \begin{cases} \alpha(t-t_0)^n + c, & t > t_0. \\ c & t < t_0. \end{cases} \quad (1)$$

The best-fit explosion time is t_0 = 60 234.19 ± 0.31 MJD (17/10/2023). In Fig. A.1 we show the power-law fitting for the r and g bands, along with the best-fit parameters. The power-law indices are n_r = 1.31 ± 0.11 and n_g = 1.51 ± 0.17 for the r and g bands, respectively, in agreement with those of the SN Iax SN 2020udy and SN 2024pxl (Maguire et al. 2023; Hoogendam et al. 2025), and slightly lower than those of the majority of normal SNe Ia ($n_r \sim 2.0$ and $n_g \sim 2.1$; Miller et al. 2020). To determine the date when the light curve reaches its maximum luminosity in the B band (t_{max}) and to derive other properties of the supernova, we used the SuperNovae in object-oriented Python (SNooPy, v2.7.2; Burns et al. 2011, 2014) fitter for the $BVgri$, r_{ZTF}, g_{ZTF} bands. `SNooPy` fits the light curves for all available filters using light-curve templates trained on the first and second stages of the CSP (Krisciunas et al. 2017, Phillips et al. 2019). It determines the time of maximum light in the B band, the $\Delta m_{15}(B)$ parameter, inferred from all bands, and the magnitude at maximum in each band, when the 'max_model' is used. `SNooPy` also estimates the s_{BV} parameter, which characterises the colour evolution relative to a typical SN Ia, where the time difference between B_{max} and $(B-V)$max is 30 days.

For the light-curve fitting, we used a 91bg template with (a) the `max_model`, which fits the whole light curve in each band independently of the other bands; (b) the `EBV_model2`, which performs multi-band fits assuming a colour law so that all bands are fitted simultaneously; and (c) the `color_model`, in which intrinsic colours from Burns et al. (2014) are used to infer the amount of extinction $E(B-V)$ and the shape of the reddening law R_V. The fits of the three different models are plotted, together with the data, in Fig. A.2. The time of B-band maximum is MJD = 60 245.8 ± 0.4 for all three models (within uncertainties), corresponding to a rise time of 11.6 ± 0.5 days, consistent with the lower end of the rise-time distribution of most SNe Ia and 91bg-like SNe (e.g. Galbany et al. 2019; Miller et al. 2020).

The colour-stretch parameter s_{BV} is 0.448 ± 0.031, 0.449 ± 0.031, and 0.449 ± 0.031 for the `max`, `EBV2`, and `color` models, respectively. The decline-rate parameter $\Delta m_{15}(B)$ is 1.885 ± 0.005 mag, as calculated using the `max_model`. The host-galaxy extinction is $E(B-V)_{host}$ = 0.353±0.066 and 0.355±0.062 mag for the `EBV2` and colour models, respectively. Finally, the shape of the host-galaxy reddening law is R_v = 2.1 ± 0.5, as derived from the `color_model`. A more detailed discussion of the host-galaxy extinction is presented in Sect. 4.2. Although the overall `SNooPy` template fitting is reasonable, we note that in the r-band SN 2023vjh rises more slowly than the template, resulting in a broader light curve, while the i-band light curve is narrower than predicted.

4.2. Extinction from the host galaxy

Given that SN 2023vjh is located at a large projected distance of 6.8 kpc from the bulge of its elliptical host galaxy (Fig. 1), and that the host is an elliptical galaxy, one would expect little or no extinction (although CSM or a non-negligible line-of-sight contribution cannot be ruled out). However, not all methods or indicators consistently support a scenario of negligible extinction. In the following, we present the different approaches we explored in order to determine whether significant extinction could be present, possibly due to CSM around the progenitor, or whether SN 2023vjh shows intrinsic reddening, which would make it an unusual case.

The first method we used was the `SNooPy` fitting with the `EBV_model2` and `color_model`. These models give $E(B-V)_{\rm host}$ = 0.353 ± 0.066 and 0.355 ± 0.062 mag, respectively. Such values are uncommon for 91bg-like SNe, for which the host extinction is typically low, usually $E(B-V)_{\rm host} < 0.1$ mag, with only a few known exceptions. For instance, in the sample of 14 91bg-like SNe presented by Graur (2024), only one object has a reported host extinction exceeding 0.1 mag ($E(B-V)_{\rm host}$ = 0.17 ± 0.08 mag), and none of the objects has $E(B-V)_{\rm host} >$ 0.2 mag.

Burns et al. (2014) proposed an updated version of the Lira law (Lira et al. 1998; Folatelli et al. 2010) that is also valid for fast-declining SNe Ia such as 91bg-like events. Using this updated Lira relation (Eq. (6) in Burns et al. 2014) at t = 45 days, we obtain $E(B-V)_{\rm host}$ = 0.20 ± 0.05. This value is lower than that inferred from the `SNooPy` fits, but still relatively high given the location of SN 2023vjh within its host galaxy.

On the other hand, the spectra provide no evidence of host-galaxy extinction. In particular, no Na I D absorption is detected in any of the spectra of SN 2023vjh. In Fig. A.3 we show several high signal-to-noise spectra, where the expected positions of the Na I D absorption lines are indicated. No absorption feature associated with the host galaxy is visible, supporting the scenario of negligible extinction along the line of sight within the host (similarly to the 91bg-like SN 2015bo; Hoogendam et al. 2022). We derive a 3σ upper limit on the equivalent width (EW) of the Na I D absorption line from the smoothed spectrum (to avoid variations due to noise) of <0.53 Å (or 0.058 ± 0.159 Å), estimated through Monte Carlo simulations that propagate flux uncertainties and continuum-placement variations.

As additional test, we compared the MW extinction-corrected light curves of SN 2023vjh with the models of Blondin et al. (2018): DDC25, a Chandrasekhar-mass WD exploding via a delayed deflagration-to-detonation transition, and SCH2p0, a sub-Chandrasekhar-mass WD undergoing a pure central detonation. Finally, we applied the circumstellar dust (CSM) extinction law of Goobar (2008) for both MW- and Large Magellanic Cloud (LMC)-type dust. This CSM extinction law accounts for scattering by dust surrounding the progenitor system, which produces a steeper, low-R_V extinction curve than standard interstellar dust. It is approximated by $A_\lambda = A_V(1-\alpha+\alpha(\lambda/\lambda_V)^p)$, with $p = -1.5, -2.5$ and $\alpha = 0.9, 0.8$ for interstellar dust in MW and LMC respectively, leading to stronger attenuation at bluer wavelengths. To test the effect of host extinction, we applied the circumstellar dust extinction law of Goobar (2008) to the light curves after correcting for MW extinction. Assuming $E(B-V)_{\rm host} = 0.2$ we obtain A_v = 0.58, 0.35 for MW and LMC dust models respectively.

In Fig. 4, we present the light curves of the two models from Blondin et al. (2018), DDC25 and SCH2p0, compared to SN 2023vjh under three extinction assumptions: (i) correcting only for MW extinction; (ii) correcting also for host-galaxy extinction with $E(B-V)_{\rm host} = 0.2$ as suggested by the Lira law; and (iii) applying the CSM extinction law of Goobar (2008) only for MW interstellar dust which provides a better match to the data.

The i band remains comparatively fainter than the model predictions even after these corrections. Given that extinction effects are expected to vary smoothly with wavelength, a residual confined primarily to a single red band is less straightforward to attribute solely to reddening uncertainties. This may instead reflect limitations in the model spectral energy distribution in the red/NIR regime, where line-blanketing and Ca II NIR triplet absorption can have a strong impact on the observed flux. In addition, we observe a slight discrepancy in the B band as well.

These results suggest that the overall faintness of SN 2023vjh is likely driven by a combination of extinction effects and band-dependent spectral modelling uncertainties. SN 2023vjh is therefore consistent with a fast-declining, subluminous SN Ia showing possible signs of additional dust or circumstellar material, while the residual tension in the i band highlights the need for improved modelling in the red part of the spectrum. Since it is unclear which scenario is more likely, we adopt a correction only for MW extinction in the following analysis which is $E(B-V)_{MW}$ = 0.236 ± 0.008 mag.

4.3. Comparison to light curves of other SNe Ia

Figure 5 shows the light curve of SN 2023vjh compared with those of several other SNe Ia: the normal SNe Ia 2011fe (Richmond & Smith 2012) and 2020jgl (Galbany et al. 2025), the transitional SN 1986G (Phillips et al. 1987), the 2002es-like SN 2002es (Ganeshalingam et al. 2012), and a small illustrative subsample of 91bg-like SNe: 1991bg (Filippenko et al. 1992; Leibundgut et al. 1993; Turatto et al. 1996; Krisciunas et al. 2004b), 1999by (Ganeshalingam et al. 2010; Garnavich et al. 2004), 2005bl (Taubenberger et al. 2008; Friedman et al. 2015; Hicken et al. 2009; Contreras et al. 2010), 2005ke (Friedman et al. 2015; Hicken et al. 2009; Contreras et al. 2010; Krisciunas et al. 2017), 2006bd (Morrell et al. 2006), 2006mr (Contreras

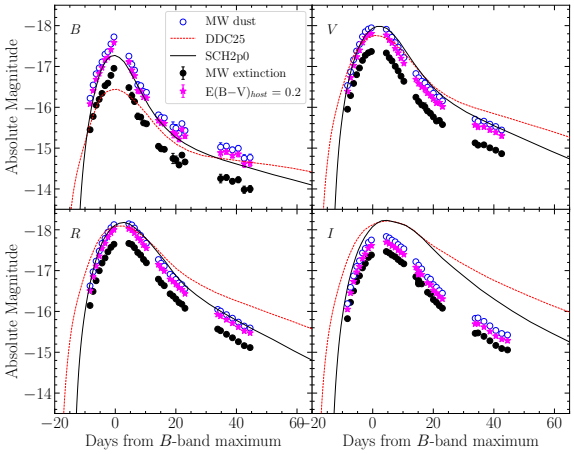


Fig. 4. Light curves of the DDC25 and SCH2p0 models from Blondin et al. (2018) compared to SN 2023vjh under three extinction assumptions: (i) correcting only for Milky Way extinction; (ii) correcting also for host-galaxy extinction with $E(B-V)_{\rm host} = 0.2$, as suggested by the Lira law (Burns et al. 2014); and (iii) applying the CSM extinction law of Goobar (2008) for Milky-Way interstellar dust. In all cases the light curves were corrected for the Milky Way extinction.

et al. 2010; Stritzinger et al. 2011), 2007N (Lee & Li 2007), 2021qvv (Graur et al. 2023), and 2022xkq (Pearson et al. 2024). In later sections, we consider these and additional 91bg-like SNe Ia for a more comprehensive comparison with SN 2023vjh. Overall, the light curve of SN 2023vjh is generally consistent with those of the other 91bg-like SNe. It appears to evolve more slowly than SNe 2006mr, 2005ke, 1999by, and 1991bg, while it more closely follows the light curves of 2005bl, 2007N, and 2006bd.

In Fig. 6, the left panel shows the B-band absolute magnitude as a function of $\Delta m_{15}(B)$ for SNe Ia from the CSP-I sample (Krisciunas et al. 2017) and the sample of 91bg-like SNe Ia from Graur (2024). The lower-right region of the diagram is populated by the subluminous, fast-declining 91bg-like SNe Ia, where SN 2023vjh is also located. We show the location of SN 2023vjh assuming only MW extinction correction as a red filled star, and as a red open star when CSM extinction from Goobar (2008) for MW-type dust is included. The right panel presents the B-band absolute magnitude as a function of the colour-stretch parameter s_{BV}. In both diagrams, and under both extinction assumptions, SN 2023vjh lies well within the locus of 91bg-like SNe Ia.

4.4. Colour curves

Figure 7 shows the MW extinction-corrected $B-V$, $g-r$, and $r-i$ colour curves of SN 2023vjh (top). The bottom panel presents the $B-V$ colour curve of SN 2023vjh corrected for MW extinction, compared with other SNe that are also corrected only for MW extinction (91bg-like SNe Ia, a 2002es-like SN, and a normal SN Ia). Although our colour coverage does not extend far in time (up to ∼40 days after maximum), the evolution of SN 2023vjh closely follows that of the other 91bg-like SNe, particularly between $B_{\rm max}$ and $(B-V)_{\rm max}$. Overall, it tends to display slightly bluer $(B-V)$ colours than most objects in this class. This may also be related to the slight discrepancy between the observed B-band light curve and the model predictions shown in Fig. 4.

Taking advantage of the high cadence of the observations, we calculated the colour-stretch parameter s_{BV} from the $B-V$ colour curve. We determined the $(B-V)_{max}$ by fitting a smoothed cubic spline to the colour curve. A smoothing factor of 25 was

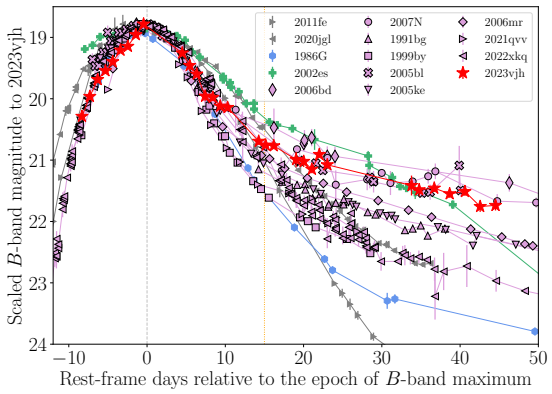


Fig. 5. Light curve of SN 2023vjh (red line) in comparison with light curves of other 91bg-like SNe (SN 2006bd, SN 2007N, SN 1991bg, SN 1999by, SN 2005bl, SN 2005ke, SN 2006mr, SN 2021qvv, SN 2022xkq, shown in purple); the normal SNe Ia SN 2011fe and SN 2020jgl (shown in grey); the transitional SN 1986G (in blue); and the SN 2002es (in green). The gray vertical dashed-line at zero corresponds to the B-band maximum, while the orange dotted line indicates the epoch +15 (references for the SNe are given in Sect. 4.3).

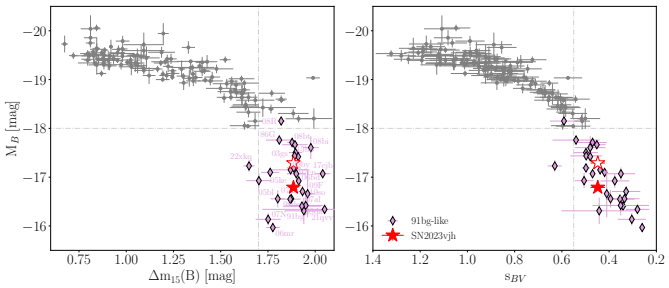


Fig. 6. Luminosity width relation as a function of Δm_{15}(B) (left) and s_{BV} (right) for a selection of CSP-I SNe Ia from Krisciunas et al. (2017) and the sample of Graur (2024) with the addition of SN 2023vjh taking into account only the MW extinction correction (red filled star) and assuming an CSM extinction from Goobar (2008) (red open star). The purple diamonds represent 91bg-like SNe.

adopted after testing various values to suppress small-scale fluctuations while preserving the global colour evolution. The epoch of maximum colour was defined as the time at which the fitted spline reaches its maximum value and the colour-stretch parameter was computed as $s_{BV} = t_{max}(B-V)/30$ (Burns et al. 2014). Uncertainties on s_{BV} were estimated via Monte Carlo resampling. The $B-V$ measurements were perturbed according to their uncertainties, the spline fitting and peak determination were repeated for 500 realisations using the same smoothing factor, and the standard deviation of the resulting s_{BV} distribution was adopted as the uncertainty. We found $s_{BV} = 0.45 \pm 0.17$, in excellent agreement with the value derived from `SNooPy`'s best-fit parameters.

Finally, in Fig. 8 we present the colour stretch parameter s_{BV} as a function of $t^i_{max} - t^B_{max}$ for various sub-types of SNe Ia. This method was suggested by Ashall et al. (2020) to photometrically differentiate between various sub-types of. SN 2023vjh lies well within the 91bg-like region, which is generally characterised by lower s_{BV} values compared to other subtypes.

4.5. Hubble constant estimate

We also estimate the value of the Hubble constant using SN 2023vjh, following the approach presented by Phillips et al. (2026), which was specifically developed for fast-declining

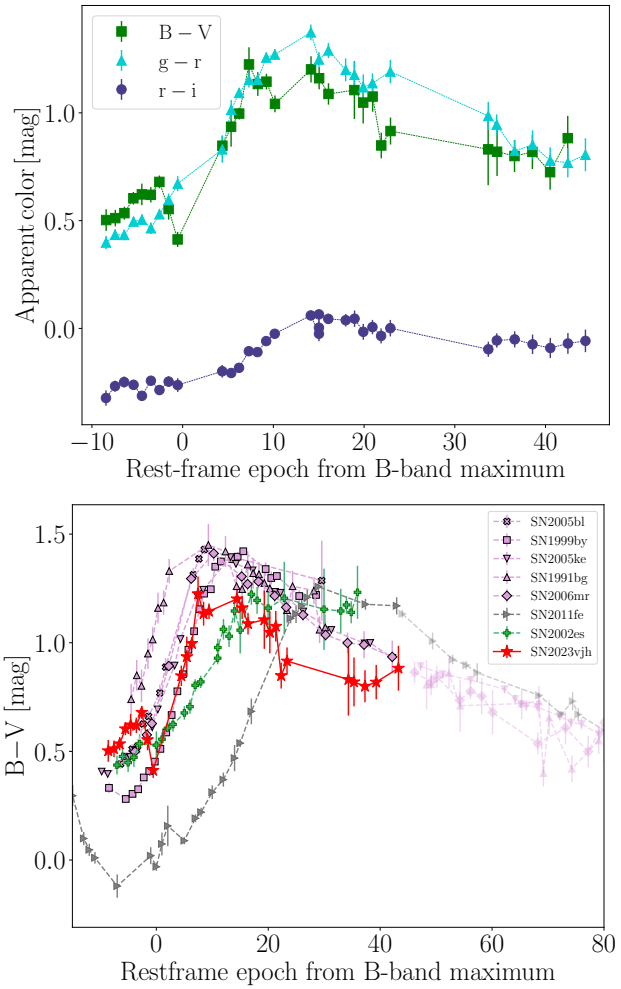


Fig. 7. Milky Way extinction-corrected colour curves of SN 2023vjh (top panel) and the MW extinction-corrected $B - V$ colour curve of SN 2023vjh in comparison with those of the 91bg-like sample, the normal SN Ia SN 2011fe, and the SN 2002es (bottom panel).

SNe Ia. In that work, two methods are proposed to standardise the luminosities of such objects: the classical Tripp relation (Tripp 1998), which combines light-curve shape and colour information, and the colour method, which uses the colour at maximum light as a luminosity indicator. In these methods, the distance moduli are computed following Eqs. (1) and (5) of Phillips et al. (2026):

$$\mu_{Tripp} = m_x - P_x^N(s_{BV-0.5}) - \beta_x(B_{max} - V_{max} - 0.4) \quad (2)$$

and

$$\mu_{color} = m_x - P_x^N(B_{max} - V_{max} - 0.4), \quad (3)$$

where m_x is the peak apparent magnitude in filter x, P_x^N denotes an N-th order polynomial (we adopt N=2) and β_x is the slope of the luminosity-colour relation). The coefficients of P_x^N and the values of β_x are taken from Table 4 of Phillips et al. (2026).

Using these calibrations, we compute the value of H_0 in each available photometric band and derive weighted averages for both methods. The resulting values are $H_0 = 71.56 \pm 3.09$ km s^{-1} Mpc^{-1} from the Tripp method and $H_0 = 74.60 \pm 2.22$ km s^{-1} Mpc^{-1} from the colour method. Figure 9 shows the values obtained in each filter together with the weighted averages and the ranges reported by Phillips et al. (2026).

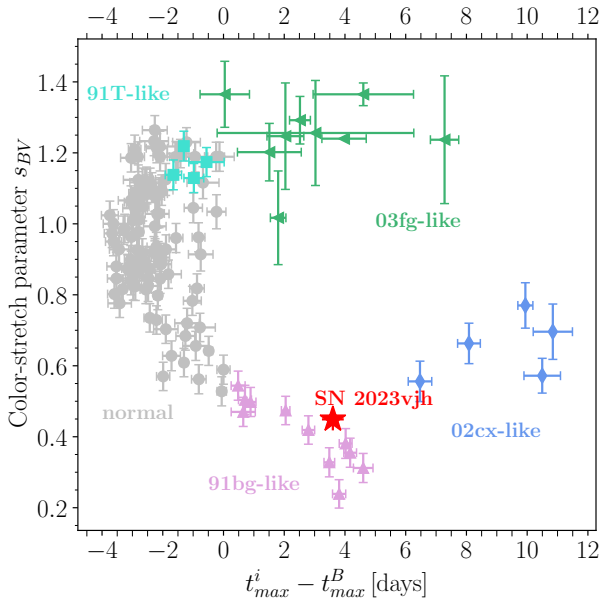


Fig. 8. Colour-stretch parameter s_{BV} as a function of $t^i_{max} - t^B_{max}$ for different sub-types of SN Ia (Ashall et al. 2020). The $t^i_{\rm max}$ and $t^B_{\rm max}$ refer to the epochs of maximum light in the i and B bands, respectively.

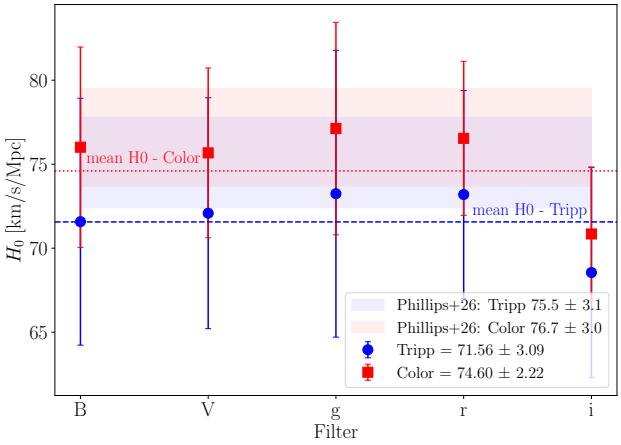


Fig. 9. Hubble constant we derived from SN 2023vjh using both the Tripp method (Tripp 1998) and the colour method (Phillips et al. 2026). For comparison, we also include the values reported by Phillips et al. (2026) for fast-declining SNe Ia.

Both estimates are consistent within the uncertainties with the values reported by Phillips et al. (2026). The colour method result lies somewhat closer to their measurement, while the Tripp-based estimate falls towards the lower end of the reported range. We note that the i-band systematically yields lower values of H_0, consistent with the fainter i-band light curve of SN 2023vjh compared to the templates.

5. Spectroscopic properties

In this section, we describe the observed spectroscopic properties of SN 2023vjh and compare them with those of other 91bg-like SNe. The rest-frame optical spectra, corrected for MW extinction, are presented in Fig. 10. The original spectra are shown in grey, the smoothed spectra in black.

The available spectra cover phases from approximately −9 to +47 days relative to the B-band maximum. The spectra

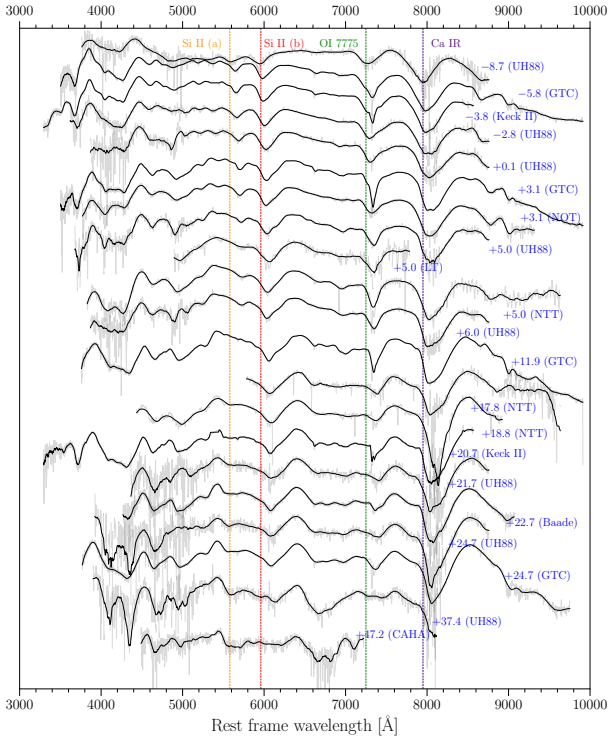


Fig. 10. Optical spectra of SN 2023vjh. Here there are 21 observations for 17 different dates. The original rest-frame spectra, corrected for colour and Milky Way extinction, are shown in grey, while the smoothed spectra are shown in black. The blue labels next to each spectrum denote the telescope and phase relative to the B maximum.

exhibit prominent absorption features due to Ca II H&K, Si II $\lambda\lambda$5972, 6355, O I λ7775, and Ca II IR triplet, which become visible around −6 day. The Si II λ5972 feature disappears around day +6, while the remaining lines gradually fade by day +19.

In Fig. 11, we compare the spectrum around the *B*-band maximum of SN 2023vjh with those of SN 1991bg (Filippenko et al. 1992), the transitional SN 1986G (Phillips et al. 1987), and the normal SN 2011fe (Nugent et al. 2011). SN 2023vjh shows spectral features very similar to SN 1991bg, whereas, compared to the other two SNe, we notice differences in the 4000–4300 Å range, where 91bg-like SNe are dominated by deep Ti II ∼ 4150 Å feature and consequently, SN 1986G and SN 2011fe show lower equivalent widths. In addition, the Si II λ5972 absorption line is stronger in SN 2023vjh and SN 1991bg compared to the others, as first reported for fast-declining (low-luminosity) SNe by Nugent et al. (1995) (also Hachinger et al. 2008).

5.1. Ejecta velocities and pseudo-equivalent widths

We estimated the expansion velocities of Ca II IR, Si II $\lambda\lambda$5972, 6355, O I λ7775, and Ca II H&K using a modified version of the SPEXTRACTOR code (Papadogiannakis 2019). This revised version (Burrow et al. 2020) performs spectral downsampling while conserving photon counts to reduce computational cost. The GP-based smoothing procedure was also refined to produce a more reliable representation of each spectrum, improving the measurements of expansion velocities and pEWs. Velocities are obtained from the wavelength shifts of absorption features using the relativistic Doppler formula given in Eq. (6) of Blondin et al. (2006), with ejecta velocities determined from the minima of the absorption lines relative to their rest wavelengths. The derived velocities are listed in Table A.3 and plotted in Fig. 12.

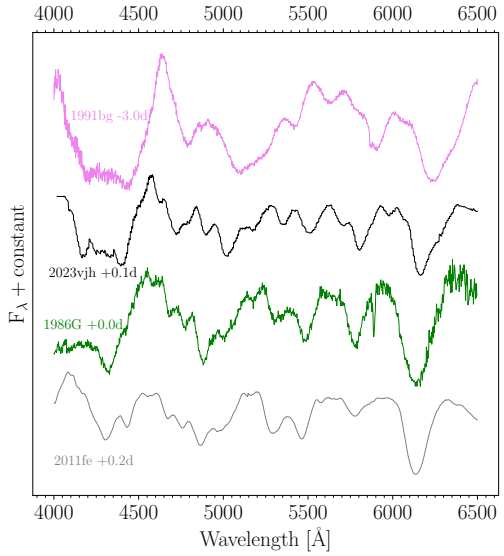


Fig. 11. Optical spectrum of SN 2023vjh obtained around the epoch of the *B*-band maximum compared with similar epoch spectra of SN 1991bg, the transitional SN 1986G, and the normal SN 2011fe.

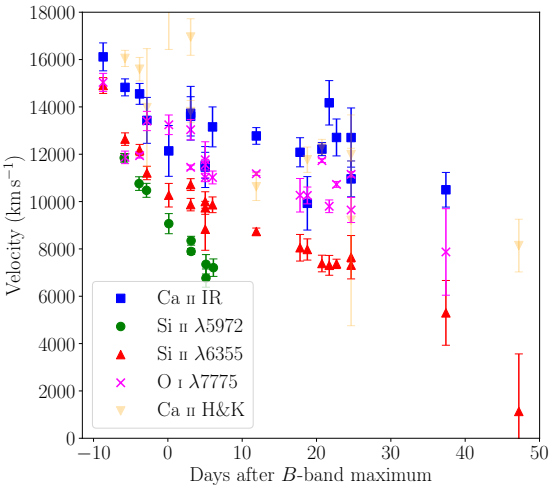


Fig. 12. Evolution of the expansion velocities.

For the absorption lines of Si II $\lambda\lambda$5972, 6355, O I λ7773, and Ca II H&K, we also measured the pseudo-equivalent widths (*pEW*). We used a simple Monte Carlo routine where the continuum points on either side of the feature were allowed to vary within ±10−30 Å (depending on the spectrum) of their nominal wavelengths. For each iteration, the nearest flux values to these perturbed positions were taken to define a linear continuum, and the spectrum was normalised with respect to it. The *pEW* was then calculated by integrating the normalised absorption profile across the chosen wavelength range. This process was repeated 1000 times, and the final *pEW* and uncertainty were taken as the mean and standard deviation of the resulting distribution. The *pEW*s are reported in Table A.3 (in parentheses) and whose evolution is also shown in Fig. 13.

5.2. Near-infrared spectra

Near-infrared spectroscopy is a powerful tool to study SN Ia physics because it allows different layers of the ejecta to be probed simultaneously (Ashall et al. 2019). Key spectral features, including C I and Mg II lines tracing unburned material and carbon burning (Hsiao et al. 2013; Marion et al. 2006), and the

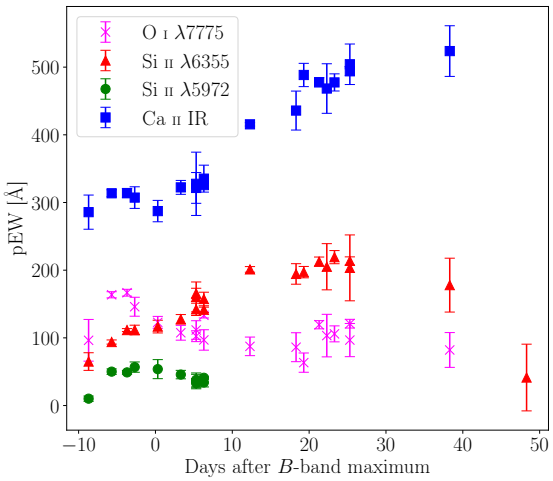


Fig. 13. Evolution of the pseudo-equivalent widths.

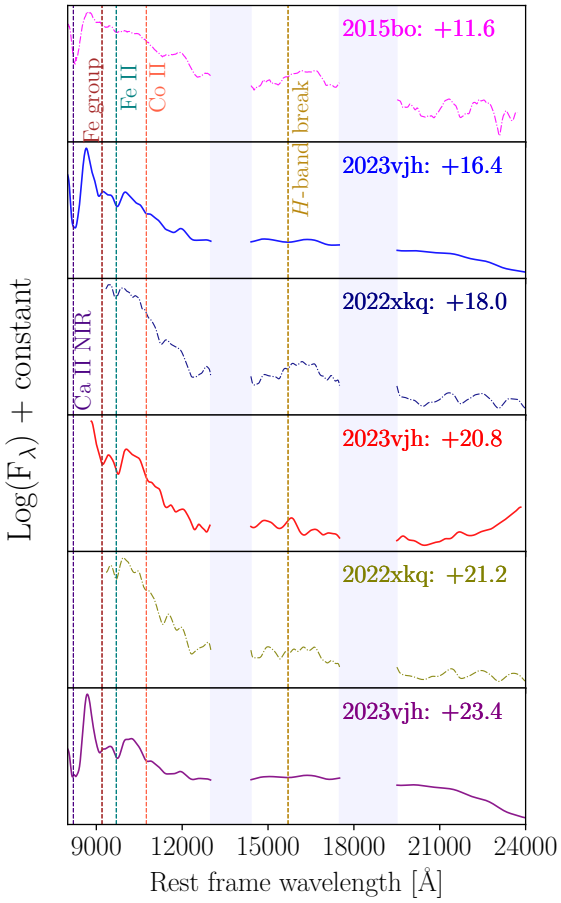


Fig. 14. Near-infrared spectra of SN 2023vjh corrected for Milky Way extinction and shifted to the rest frame compared with those of SN 2022xkq at similar epochs. Light-blue shaded regions indicate wavelength ranges affected by strong telluric absorption, which have been excluded from the plotted spectra.

iron-peak H-band emission, connect spectroscopic observables directly to explosion physics. The H-band emission is linked to ^{56}Ni production and light-curve properties, and it also provides a probe of the temperature of the line-blanketing material (Wheeler et al. 1998; Hsiao et al. 2013).

The NIR spectra of SN 2023vjh are shown in Fig. 14. A Gaussian smoothing with σ = 15−20 has been applied. The most prominent absorption feature is found at 8150–8300 Å and corresponds to the Ca II NIR triplet (8500, 8540, 8660 Å), also visible in the optical spectra shown in Fig. 10. This absorption feature includes contributions from Co II and Mn II; however, the Ca II contribution is much stronger. The expansion velocities of Ca II NIR are presented in Table A.3.

Table 2. Expansion velocities of the features associated with Fe II (9900 Å) and Co II (10910 Å) in the NIR spectra.

Epoch (days)	vCo II (km s^{-1})	vFe II (km s^{-1})
+16.4	4399 ± 540	2983 ± 432
+20.8	2401 ± 1023	1153 ± 374
+23.4	3969 ± 957	2295 ± 468

Since our spectra were obtained at relatively late phases, the Mg II doublet (9220–9240 Å) is no longer present. Mg II forms in the outer layers of the ejecta (as a product of explosive carbon burning), and as the ejecta expand the column density decreases rapidly. As a result, the Mg II feature fades and becomes undetectable a few days after maximum light (e.g. Marion et al. 2003). Then the spectrum in this region is dominated by Co II (8550 Å) and Mn II (9440 Å). However, at later times this region is dominated by blended iron-group lines, while Mn II is not detectable anymore. Hence, the absorption feature seen around 9100 Å is most probably due to Fe-group lines. Finally, we observe two more absorption features around 9900 and around 10910 Å, in all three spectra, which are due to Fe II and Co II respectively. The velocities corresponding to the feature minima are listed in Table 2.

In Fig. 10 we also include NIR spectra of the 91bg-like SN 2015bo (Hoogendam et al. 2022) and SN 2022xkq (Pearson et al. 2024) at epochs similar to those of SN 2023vjh (a Gaussian smoothing has also been applied with σ = 2 for SN 2015bo and 20 for SN 2022xkq). The same spectral features are present in all objects. However, Pearson et al. (2024) report that the prominent iron-peak emission in the H band, which begins to appear ∼5 days after B-band maximum, has a blue-edge velocity ($v_{\rm edge}$) of −5500 km s^{-1} at epoch +21 (Ashall et al. 2019). The H-band feature is also apparent in the spectrum of SN 2015bo. In contrast, no H-band break is apparent in our spectra. It is unclear whether this is due to the lower S/N at those wavelengths or the actual absence of the feature.

Finally, we examined the position of SN 2023vjh in several classification diagrams, using both its photometric and spectroscopic properties. In all cases, it lies within the locus of 91bg-like SNe Ia and cool SNe, and more specifically, it is consistent with the sub-class of extremely cool SNe. A more detailed discussion of these classification diagrams is provided in Appendix B.

6. Summary and conclusions

We have presented observations of the 91bg-like supernova SN 2023vjh discovered on 17 October 2023 and with a rise time of 11.6 days. The best-fit light-curve parameters are $\Delta m_{15}(B)$ = 1.89 ± 0.01 and s_{BV} = 0.45 ± 0.03, which together with the apparent B-band magnitude at maximum place SN 2023vjh firmly within the locus of 91bg-like SNe in the luminosity–width relation diagram.

Optical spectra spanning −8.6 to +47.3 days relative to the B-band maximum show the typical 91bg-like features, including Si II, Ca II, O I, and Ti II. Measured expansion velocities

and pseudo-equivalent widths confirm that SN 2023vjh is an extremely cool event, consistent with the definition of Folatelli et al. (2013). In addition, late-phase NIR spectra at three epochs revealed Ca II IR, Fe II, and Co II absorption features, complementing the optical dataset, and the H-band break feature is absent.

What makes SN 2023vjh particularly peculiar among 91bg-like SNe is its dimness relative to both typical events and explosion models combined with indications of higher than usual reddening ($E(B-V)_{\rm host}$ ~0.2–0.35). On the other hand, the lack of Na I D absorption and its location at 6.8 kpc from the bulge of its passive elliptical host suggest minimal interstellar extinction.

We compared the observed light curves with the Chandrasekhar-mass delayed-detonation model DDC25 and the sub-Chandrasekhar-mass central detonation model SCH2p0 from Blondin et al. (2018). We further tested the impact of circumstellar dust using the low-R_V, scattering-dominated extinction law of Goobar (2008) for Milky Way- and LMC-type dust. We find that the combination of the sub-Chandrasekhar SCH2p0 model with MW-type CSM extinction provides the best overall match to the observed light curves, improving agreement in the blue bands. Residual discrepancies at red wavelengths likely reflect limitations in the model spectral energy distribution in the red and NIR regime, where strong line-forming features such as the Ca II NIR triplet can significantly affect the i-band flux.

These results show that SN 2023vjh is an unusually faint, fast-declining 91bg-like supernova. Its systematically fainter light curves, despite the lack of clear host-galaxy extinction signatures, make it a distinctive case within this sub-class. A contribution from circumstellar material affecting the observed reddening cannot be excluded and may represent an interesting possibility for this event.

Finally, we used SN 2023vjh to estimate the Hubble constant following the approach of Phillips et al. (2026), which is tailored for fast-declining SNe Ia. Applying both the classical Tripp relation (Tripp 1998) and the colour method, we found $H_0 = 71.56 \pm 3.09$ km s^{-1} Mpc^{-1} from the Tripp method and $H_0 = 74.60 \pm 2.22$ km s^{-1} Mpc^{-1} from the colour method. Both values are consistent within uncertainties with those from Phillips et al. (2026), with the colour method result lying slightly closer to the reference values.

Data availability

The spectra used in this work are publicly available through the WISeREP repository.

Acknowledgements. We thank the anonymous referee for the thorough review and the useful comments that helped to improve the clarity of the paper. M.K. acknowledges financial support from MICINN (Spain) through the programme Juan de la Cierva-Incorporación [JC2022-049447-I], from AGAUR, CSIC, MCIN and AEI 10.13039/501100011033 under projects PID2023-151307NB-I00, PIE 20215AT016. M.K., L.G, and M.G.B. acknowledge the program Unidad de Excelencia María de Maeztu CEX2020-001058-M, and the Departament de Recerca i Universitats de la Generalitat de Catalunya through the 2021-SGR-01270 grant. L.G. acknowledges financial support from the Spanish Ministerio de Ciencia e Innovación (MCIN) and the Agencia Estatal de Investigación (AEI) 10.13039/501100011033 under the PID2023-151307NB-I00 SNNEXT project, from Centro Superior de Investigaciones Científicas (CSIC) under projects PIE 20215AT016, ILINK23001, COOPB2304. M.D.S. is funded by the Independent Research Fund Denmark (IRFD, grant number 10.46540/2032-00022B). M.G.B. acknowledges financial support from the Spanish Ministerio de Ciencia e Innovación (MCIN) and the Agencia Estatal de Investigación (AEI) 10.13039/501100011033 under the PID2023-151307NB-I00 SNNEXT project, from Centro Superior de Investigaciones Científicas (CSIC) under projects PIE 20215AT016, ILINK23001, COOPB2304. M.G.B.'s work has been carried out within the framework of the doctoral program in Physics of the Universitat Autònoma de Barcelona. T.-W.C. acknowledges financial support from the Yushan Fellow Program of the Ministry of Education, Taiwan (MOE-111-YSFMS-0008-001-P1), and from the National Science and Technology Council, Taiwan (NSTC 114-2112-M-008-021-MY3) J.T.H. acknowledges support from NASA through the NASA Hubble Fellowship grant HST-HF2-51577.001-A, awarded by STScI. STScI is operated by the Association of Universities for Research in Astronomy, Incorporated, under NASA contract NAS5-26555. C.J. acknowledges financial support from grant PRE2021-096988 funded by AEI 10.13039/501100011033 and ESF Investing in your future. C.J. work has been carried out within the framework of the doctoral program in Physics of the Universitat Autònoma de Barcelona R.G.B. acknowledges financial support from the Severo Ochoa grant CEX2021-001131-S funded by MCIN/AEI/10.13039/501100011033 and the grant PID2022-141755NB-I00.

References

Alburai, A., Galbany, L., Burgaz, U., et al. 2026, A&A, 707, A91
Arnett, W. D. 1980, ApJ, 237, 541
Ashall, C., Hsiao, E. Y., Hoeflich, P., et al. 2019, ApJ, 875, L14
Ashall, C., Lu, J., Burns, C., et al. 2020, ApJ, 895, L3
Bellm, E. C., Kulkarni, S. R., Graham, M. J., et al. 2019, PASP, 131, 018002
Blondin, S., Dessart, L., Leibundgut, B., et al. 2006, AJ, 131, 1648
Blondin, S., Matheson, T., Kirshner, R. P., et al. 2012, AJ, 143, 126
Branch, D., Dang, L. C., Hall, N., et al. 2006, PASP, 118, 560
Blondin, S., Dessart, L., & Hillier, D. J. 2018, MNRAS, 474, 3931
Burns, C. R., Stritzinger, M., Phillips, M. M., et al. 2011, AJ, 141, 19
Burns, C. R., Stritzinger, M., Phillips, M. M., et al. 2014, ApJ, 789, 32
Burns, C. R., Parent, E., Phillips, M. M., et al. 2018, ApJ, 869, 56
Burns, C., Hsiao, E., Suntzeff, N., et al. 2021, ATel, 14441, 1
Burrow, A., Baron, E., Ashall, C., et al. 2020, ApJ, 901, 154
Buzzoni, B., Delabre, B., Dekker, H., et al. 1984, The Messenger, 38, 9
Cappellari, M. 2023, MNRAS, 526, 3273
Cappellari, M., & Emsellem, E. 2004, PASP, 116, 138
Cardelli, J. A., Clayton, G. C., & Mathis, J. S. 1989, ApJ, 345, 245
Cenarro, A. J., Peletier, R. F., Sánchez-Blázquez, P., et al. 2007, MNRAS, 374, 664
Chabrier, G. 2003, PASP, 115, 763
Contreras, C., Hamuy, M., Phillips, M. M., et al. 2010, AJ, 139, 519
Desai, D. D., Kochanek, C. S., Shappee, B. J., et al. 2024, MNRAS, 530, 5016
Desai, D. D., Shappee, B. J., Kochanek, C. S., et al. 2026, arXiv e-prints [arXiv:2602.00223]
Dimitriadis, G., Burgaz, U., Deckers, M., et al. 2025, A&A, 694, A10
Djupvik, A. A., & Andersen, J. 2010, Astrophys. Space Sci. Proc., 14, 211
Dressler, A., Bigelow, B., Hare, T., et al. 2011, PASP, 123, 288
Filippenko, A. V. 1997, ARA&A, 35, 309
Filippenko, A. V., Richmond, M. W., Branch, D., et al. 1992, AJ, 104, 1543
Fixsen, D. J., Cheng, E. S., Gales, J. M., et al. 1996, ApJ, 473, 576
Folatelli, G., Phillips, M. M., Burns, C. R., et al. 2010, AJ, 139, 120
Folatelli, G., Morrell, N., Phillips, M. M., et al. 2013, ApJ, 773, 53
Friedman, A. S., Wood-Vasey, W. M., Marion, G. H., et al. 2015, ApJS, 220, 9
Galbany, L., Anderson, J. P., Sánchez, S. F., et al. 2018, ApJ, 855, 107
Galbany, L., Ashall, C., Höflich, P., et al. 2019, A&A, 630, A76
Galbany, L., Gutiérrez, C. P., Piscarreta, L., et al. 2025, J. Cosmology Astropart. Phys., 2025, 053
Ganeshalingam, M., Li, W., Filippenko, A. V., et al. 2010, ApJS, 190, 418
Ganeshalingam, M., Li, W., Filippenko, A. V., et al. 2012, ApJ, 751, 142
García-Benito, R., Jiménez, A., Sánchez-Menguiano, L., et al. 2024, A&A, 691, A161
García-Berro, E., & Lorén-Aguilar, P. 2017, in Handbook of Supernovae, eds. A. W. Alsabti, & P. Murdin (Berlin: Springer), 1237
Garnavich, P. M., Bonanos, A. Z., Krisciunas, K., et al. 2004, ApJ, 613, 1120
Garzón, F., Balcells, M., Gallego, J., et al. 2022, A&A, 667, A107
Goobar, A. 2008, ApJ, 686, L103
Graur, O. 2024, MNRAS, 530, 4950
Graur, O., Padilla Gonzalez, E., Burke, J., et al. 2023, MNRAS, 526, 2977
Hachinger, S., Mazzali, P. A., Tanaka, M., Hillebrandt, W., & Benetti, S. 2008, MNRAS, 389, 1087
Hamuy, M., Folatelli, G., Morrell, N. I., et al. 2006, PASP, 118, 2
Hamuy, M., Phillips, M. M., Suntzeff, N. B., et al. 2003, Nature, 424, 651
Hicken, M., Challis, P., Jha, S., et al. 2009, ApJ, 700, 331
Hoeflich, P., Hsiao, E. Y., Ashall, C., et al. 2017, ApJ, 846, 58
Hoeflich, P., & Khokhlov, A. 1996, ApJ, 457, 500
Höflich, P., Gerardy, C. L., Fesen, R. A., & Sakai, S. 2002, ApJ, 568, 791
Hoogendam, W. B., Ashall, C., Galbany, L., et al. 2022, ApJ, 928, 103
Hoogendam, W. B., Ashall, C., Jones, D. O., et al. 2025, ApJ, 988, 209

Horne, K. 1986, PASP, 98, 609
Hoyle, F., & Fowler, W. A. 1960, ApJ, 132, 565
Hsiao, E. Y., Conley, A., Howell, D. A., et al. 2007, ApJ, 663, 1187
Hsiao, E. Y., Marion, G. H., Phillips, M. M., et al. 2013, ApJ, 766, 72
Hsiao, E. Y., Phillips, M. M., Marion, G. H., et al. 2019, PASP, 131, 014002
Husemann, B., Kamann, S., Sandin, C., et al. 2012, A&A, 545, A137
Iben, Jr., I., & Tutukov, A. V. 1984, ApJS, 54, 335
Jensen, J. B., Blakeslee, J. P., Ma, C.-P., et al. 2021, ApJS, 255, 21
Kaiser, N., Aussel, H., Burke, B. E., et al. 2002, SPIE, 4836, 154
Kelz, A., Verheijen, M. A. W., Roth, M. M., et al. 2006, PASP, 118, 129
Kochanek, C. S., Pahre, M. A., Falco, E. E., et al. 2001, ApJ, 560, 566
Krisciunas, K., Phillips, M. M., & Suntzeff, N. B. 2004a, ApJ, 602, L81
Krisciunas, K., Suntzeff, N. B., Phillips, M. M., et al. 2004b, AJ, 128, 3034
Krisciunas, K., Contreras, C., Burns, C. R., et al. 2017, AJ, 154, 211
Kromer, M., Pakmor, R., Taubenberger, S., et al. 2013, ApJ, 778, L18
Kromer, M., Fremling, C., Pakmor, R., et al. 2016, MNRAS, 459, 4428
Kromer, M., Sim, S. A., Fink, M., et al. 2010, ApJ, 719, 1067
Kroupa, P. 2001, MNRAS, 322, 231
Lantz, B., Aldering, G., Antilogus, P., et al. 2004, SPIE Conf. Ser., 5249, 146
Lavaux, G., & Hudson, M. J. 2011, MNRAS, 416, 2840
Lee, N., & Li, W. 2007, Central Bureau Electronic Telegrams, 818, 1
Leibundgut, B., Kirshner, R. P., Phillips, M. M., et al. 1993, AJ, 105, 301
Li, W., Leaman, J., Chornock, R., et al. 2011, MNRAS, 412, 1441
Lira, P., Suntzeff, N. B., Phillips, M. M., et al. 1998, AJ, 115, 234
Livne, E. 1990, ApJ, 354, L53
Maeda, K., Jiang, J.-a., Shigeyama, T., & Doi, M. 2018, ApJ, 861, 78
Maguire, K., Magee, M. R., Leloudas, G., et al. 2023, MNRAS, 525, 1210
Marion, G. H., Höflich, P., Vacca, W. D., & Wheeler, J. C. 2003, ApJ, 591, 316
Marion, G. H., Höflich, P., Wheeler, J. C., et al. 2006, ApJ, 645, 1392
Martin, C., Moore, A., Morrissey, P., et al. 2010, SPIE Conf. Ser., 7735, 77350M
Mazzali, P. A., Benetti, S., Altavilla, G., et al. 2005, ApJ, 623, L37
Mazzali, P. A., Chugai, N., Turatto, M., et al. 1997, MNRAS, 284, 151
McCully, C., Jha, S. W., Foley, R. J., et al. 2014, Nature, 512, 54
McCully, C., Jha, S. W., Scalzo, R. A., et al. 2022, ApJ, 925, 138
Miller, A. A., Yao, Y., Bulla, M., et al. 2020, ApJ, 902, 47
Morrell, N., Folatelli, G., & Contreras, C. 2006, Central Bureau Electronic Telegrams, 477, 1
Morrell, N., Phillips, M. M., Folatelli, G., et al. 2024, ApJ, 967, 20
Nomoto, K. 1980, Space Sci. Rev., 27, 563
Nomoto, K. 1982, ApJ, 253, 798
Nugent, P., Phillips, M., Baron, E., Branch, D., & Hauschildt, P. 1995, ApJ, 455, L147
Nugent, P. E., Sullivan, M., Cenko, S. B., et al. 2011, Nature, 480, 344
Pakmor, R., Kromer, M., Röpke, F. K., et al. 2010, Nature, 463, 61
Pakmor, R., Kromer, M., Taubenberger, S., & Springel, V. 2013, ApJ, 770, L8
Panther, F. H., Seitenzahl, I. R., Ruiter, A. J., et al. 2019, PASA, 36, e031
Papadogiannakis, S. 2019, PhD thesis, Stockholm University, Sweden
Paturel, G., Petit, C., Prugniel, P., et al. 2003, A&A, 412, 45
Pearson, J., Sand, D. J., Lundqvist, P., et al. 2024, ApJ, 960, 29
Pejcha, O., Antognini, J. M., Shappee, B. J., & Thompson, T. A. 2013, MNRAS, 435, 943
Perlmutter, S., Aldering, G., Goldhaber, G., et al. 1999, ApJ, 517, 565
Phillips, M. M. 1993, ApJ, 413, L105
Phillips, M. M., Phillips, A. C., Heathcote, S. R., et al. 1987, PASP, 99, 592
Phillips, M. M., Contreras, C., Hsiao, E. Y., et al. 2019, PASP, 131, 014001
Phillips, M. M., Uddin, S. A., Burns, C. R., et al. 2026, ApJ, 998, 101
Piascik, A. S., Steele, I. A., Bates, S. D., et al. 2014, SPIE Conf. Ser., 9147, 91478H
Piersanti, L., Tornambé, A., & Castellani, V. 2004, MNRAS, 353, 243
Planck Collaboration XIII. 2016, A&A, 594, A13
Polin, A., Nugent, P., & Kasen, D. 2019, ApJ, 873, 84
Pskovskii, I. P. 1977, Sov. Astron. Lett., 3, 215
Raiteri, C. M., Villata, M., & Navarro, J. F. 1996, A&A, 315, 105
Richmond, M. W., & Smith, H. A. 2012, J. Am. Assoc. Variable Star Observers, 40, 872
Riess, A. G., Press, W. H., & Kirshner, R. P. 1996, ApJ, 473, 88
Riess, A. G., Filippenko, A. V., Challis, P., et al. 1998, AJ, 116, 1009
Riess, A. G., Li, S., Anand, G. S., et al. 2025, ApJ, 992, L34
Roth, M. M., Kelz, A., Fechner, T., et al. 2005, PASP, 117, 620
Sánchez-Blázquez, P., Peletier, R. F., Jiménez-Vicente, J., et al. 2006, MNRAS, 371, 703
Sánchez, S. F., Kennicutt, R. C., Gil de Paz, A., et al. 2012, A&A, 538, A8
Scalzo, R. A., Aldering, G., Antilogus, P., et al. 2010, ApJ, 713, 1073
Schlafly, E. F., & Finkbeiner, D. P. 2011, ApJ, 737, 103
Schlegel, D. J., Finkbeiner, D. P., & Davis, M. 1998, ApJ, 500, 525
Shappee, B. J., & Thompson, T. A. 2013, ApJ, 766, 64
Shingles, L., Smith, K. W., Young, D. R., et al. 2021, Transient Name Server AstroNote, 7, 1
Simcoe, R. A., Burgasser, A. J., Schechter, P. L., et al. 2013, PASP, 125, 270
Smartt, S. J., Valenti, S., Fraser, M., et al. 2015, A&A, 579, A40
Steele, I. A., Smith, R. J., Rees, P. C., et al. 2004, SPIE Conf. Ser., 5489, 679
Stritzinger, M., Mazzali, P. A., Sollerman, J., & Benetti, S. 2006, A&A, 460, 793
Stritzinger, M. D., Phillips, M. M., Boldt, L. N., et al. 2011, AJ, 142, 156
Stritzinger, M. D., Valenti, S., Hoeflich, P., et al. 2015, A&A, 573, A2
Taubenberger, S. 2017, in Handbook of Supernovae, eds. A. W. Alsabti, & P. Murdin (Berlin: Springer), 317
Taubenberger, S., Hachinger, S., Pignata, G., et al. 2008, MNRAS, 385, 75
Thompson, T. A. 2011, ApJ, 741, 82
Tonry, J. L., Denneau, L., Flewelling, H., et al. 2018a, ApJ, 867, 105
Tonry, J. L., Denneau, L., Heinze, A. N., et al. 2018b, PASP, 130, 064505
Tripp, R. 1998, A&A, 331, 815
Tucker, M. A., Shappee, B. J., Vallely, P. J., et al. 2020, MNRAS, 493, 1044
Tucker, M. A., Shappee, B. J., Huber, M. E., et al. 2022, PASP, 134, 124502
Turatto, M., Benetti, S., Cappellaro, E., et al. 1996, MNRAS, 283, 1
van Kerkwijk, M. H., Chang, P., & Justham, S. 2010, ApJ, 722, L157
Vazdekis, A., Sánchez-Blázquez, P., Falcón-Barroso, J., et al. 2010, MNRAS, 404, 1639
Verheijen, M., Bershady, M., Andersen, D., et al. 2004, Astron. Nachr., 325, 151
Wang, X., Filippenko, A. V., Ganeshalingam, M., et al. 2009, ApJ, 699, L139
Webbink, R. F. 1984, ApJ, 277, 355
Wheeler, J. C., Höflich, P., Harkness, R. P., & Spyromilio, J. 1998, ApJ, 496, 908
Whelan, J., & Iben, Jr., I. 1973, ApJ, 186, 1007
Wolf, C., Onken, C. A., Luvaul, L. C., et al. 2018, PASA, 35, e010
Woosley, S. E., & Weaver, T. A. 1994, ApJ, 423, 371

[1] Institute of Space Sciences (ICE, CSIC), Barcelona, Spain
[2] Institut d'Estudis Espacials de Catalunya (IEEC), Barcelona, Spain.
[3] Instituto de Astrofísica de La Plata (IALP), CONICET, Argentina
[4] Facultad de Ciencias Astronómicas y Geofísicas (FCAG), Universidad Nacional de La Plata (UNLP), Argentina
[5] Carnegie Observatories, Las Campanas Observatory, Colina El Pino, Chile
[6] Carnegie Observatories, Pasadena, USA.
[7] Department of Physics and Astronomy, Aarhus University, Denmark
[8] Instituto de Astrofísica de Andalucía–CSIC, Granada, Spain.
[9] School of Physics, Trinity College Dublin, The University of Dublin, Dublin, Ireland
[10] Instituto de Ciencias Exactas y Naturales (ICEN), Universidad Arturo Prat Iquique, Chile
[11] Department of Physics, Florida State University, USA
[12] School of Physics, The University of Melbourne, Parkville, VIC, Australia
[13] Department of Astronomy and Astrophysics, University of California, Santa Cruz, CA, USA
[14] European Southern Observatory, Santiago, Chile
[15] Institute for Astronomy, University of Hawai'i at Mānoa, Honolulu, USA
[16] Graduate Institute of Astronomy, National Central University, Jhongli, Taiwan
[17] Sorbonne Université, Université Paris Cité, CNRS, Laboratoire de Physique Nucléaire et de Hautes Energies, Paris, France
[18] Space Telescope Science Institute, Baltimore, USA
[19] Astronomical Observatory, University of Warsaw, Warszawa, Poland
[20] Department of Astronomy, University of Illinois Urbana-Champaign, Urbana, USA
[21] NSF-Simons AI Institute for the Sky (SkAI), Chicago, USA
[22] Department of Physics and Astronomy, University of Turku, Finland
[23] Astrophysics Research Institute, Liverpool John Moores University, Liverpool, UK
[24] Max-Planck-Institut für Astrophysik, Garching, Germany
[25] Carnegie Observatories, Las Campanas Observatory, Casilla 601, La Serena, Chile
[26] Instituto de Alta Investigación, Universidad de Tarapacá, Casilla 7D, Arica, Chile
[27] Department of Physics and Astronomy, Purdue University, 525 Northwestern Avenue, West Lafayette, IN 47907, USA
[28] Center for Cosmology and Astroparticle Physics, The Ohio State University, Columbus, USA
[29] Astrophysics Research Centre, Queen's University Belfast, Belfast, UK

Appendix A: Photometric and spectral log and properties

Table A.1: SWOPE photometry log.

MJD	Epoch (days)	B (mag)	V(mag)	g (mag)	r (mag)	i (mag)
60237.27	−8.49	20.287 ± 0.043	19.450 ± 0.026	19.798 ± 0.024	19.134 ± 0.019	19.270 ± 0.030
60238.29	−7.47	19.962 ± 0.032	19.116 ± 0.021	19.489 ± 0.019	18.789 ± 0.016	18.870 ± 0.020
60239.31	−6.45	19.687 ± 0.025	18.818 ± 0.017	19.227 ± 0.017	18.528 ± 0.017	18.590 ± 0.019
60240.35	−5.41	19.543 ± 0.024	18.605 ± 0.017	19.043 ± 0.019	18.282 ± 0.013	18.357 ± 0.020
60241.3	−4.46	19.397 ± 0.045	18.441 ± 0.022	18.864 ± 0.019	18.094 ± 0.015	18.220 ± 0.018
60242.31	−3.45	19.208 ± 0.030	18.254 ± 0.019	18.700 ± 0.022	17.970 ± 0.015	18.026 ± 0.017
60243.27	−2.49	19.146 ± 0.027	18.132 ± 0.012	18.614 ± 0.017	17.819 ± 0.016	17.918 ± 0.017
60244.3	−1.46	18.956 ± 0.034	18.068 ± 0.035	18.571 ± 0.024	17.710 ± 0.018	17.770 ± 0.017
60245.32	−0.44	18.783 ± 0.031	18.036 ± 0.016	18.571 ± 0.027	17.634 ± 0.022	17.710 ± 0.023
60250.33	4.57	19.255 ± 0.037	18.073 ± 0.029	18.709 ± 0.059	17.613 ± 0.019	17.625 ± 0.022
60251.33	5.57	19.458 ± 0.088	18.188 ± 0.028	18.921 ± 0.042	17.641 ± 0.016	17.661 ± 0.014
60252.22	6.46	19.598 ± 0.025	18.267 ± 0.011	19.075 ± 0.015	17.717 ± 0.013	17.713 ± 0.013
60253.32	7.56	19.958 ± 0.077	18.399 ± 0.020	19.253 ± 0.033	17.835 ± 0.012	17.754 ± 0.015
60254.3	8.54	19.978 ± 0.052	18.510 ± 0.018	19.317 ± 0.022	17.898 ± 0.010	17.821 ± 0.011
60255.27	9.51	20.120 ± 0.033	18.641 ± 0.015	19.529 ± 0.021	18.007 ± 0.011	17.879 ± 0.012
60256.23	10.47	20.142 ± 0.036	18.766 ± 0.015	19.624 ± 0.022	18.088 ± 0.013	17.926 ± 0.011
60260.28	14.52	20.693 ± 0.056	19.157 ± 0.024	20.128 ± 0.033	18.489 ± 0.015	18.242 ± 0.016
60261.19	15.43	20.755 ± 0.047	19.260 ± 0.021	20.093 ± 0.031	18.580 ± 0.015	18.418 ± 0.031
60262.24	16.48	20.767 ± 0.044	19.345 ± 0.023	20.204 ± 0.031	18.649 ± 0.017	18.418 ± 0.017
60263.32	17.56	···	19.390 ± 0.094	···	···	···
60264.19	18.43	···	19.492 ± 0.047	20.313 ± 0.049	18.848 ± 0.020	18.623 ± 0.021
60265.18	19.42	20.991 ± 0.125	19.551 ± 0.048	20.344 ± 0.055	18.902 ± 0.022	18.670 ± 0.031
60266.17	20.41	21.021 ± 0.091	19.639 ± 0.033	20.358 ± 0.056	18.974 ± 0.021	18.803 ± 0.030
60267.21	21.45	21.149 ± 0.065	19.739 ± 0.027	20.465 ± 0.040	19.062 ± 0.022	18.869 ± 0.025
60268.18	22.42	20.908 ± 0.051	19.725 ± 0.031	···	19.102 ± 0.023	18.950 ± 0.026
60269.22	23.46	21.076 ± 0.056	19.826 ± 0.028	20.659 ± 0.047	19.202 ± 0.027	19.014 ± 0.027
60280.21	34.45	21.414 ± 0.162	20.249 ± 0.037	20.964 ± 0.060	19.713 ± 0.026	19.623 ± 0.024
60281.18	35.42	21.484 ± 0.105	20.330 ± 0.040	20.962 ± 0.042	19.751 ± 0.022	19.620 ± 0.025
60283.18	37.42	21.457 ± 0.062	20.323 ± 0.040	20.928 ± 0.041	19.839 ± 0.027	19.703 ± 0.026
60285.18	39.42	21.549 ± 0.064	20.396 ± 0.047	21.042 ± 0.058	19.925 ± 0.034	19.812 ± 0.030
60287.17	41.41	21.513 ± 0.071	20.454 ± 0.039	21.065 ± 0.053	20.021 ± 0.032	19.925 ± 0.034
60289.15	43.39	21.756 ± 0.088	20.539 ± 0.054	21.152 ± 0.060	20.118 ± 0.032	20.001 ± 0.036
60291.13	45.37	21.738 ± 0.083	···	21.236 ± 0.067	20.165 ± 0.037	20.036 ± 0.037

Table A.2: ZTF r, g and ATLAS c, o, photometry

MJD	Epoch (days)	ZTF r (mag)	ZTF g (mag)	ATLAS o (mag)	ATLAS c (mag)
60234.38	−11.38	20.639 ± 0.152	21.105 ± 0.203	···	···
60235.49	−10.27	···	···	···	19.720 ± 0.139
60236.38	−9.38	19.609 ± 0.063	20.180 ± 0.089	···	···
60237.47	−8.29	···	···	···	19.510 ± 0.155
60238.39	−7.37	18.707 ± 0.029	19.387 ± 0.044	···	···
60239.47	−6.29	···	···	···	18.779 ± 0.057
60241.41	−4.35	18.107 ± 0.024	18.836 ± 0.046	18.176 ± 0.049	···
60242.2	−3.56	···	···	18.080 ± 0.074	···
60244.35	−1.41	17.660 ± 0.022	18.471 ± 0.057	···	···
60245.37	−0.39	···	···	17.968 ± 0.313	···
60246.36	0.6	17.614 ± 0.039	18.420 ± 0.085	···	···
60249.51	3.75	···	18.727 ± 0.158	···	···
60251.41	5.65	17.624 ± 0.016	18.990 ± 0.056	17.635 ± 0.029	···
60253.34	7.58	17.750 ± 0.016	19.193 ± 0.046	17.826 ± 0.036	···
60254.21	8.45	···	···	17.834 ± 0.053	···
60257.36	11.6	18.328 ± 0.055	19.928 ± 0.099	···	19.014 ± 0.076
60259.42	13.66	18.292 ± 0.025	20.141 ± 0.127	···	19.119 ± 0.080
60260.29	14.53	···	···	18.353 ± 0.129	···
60261.39	15.63	18.493 ± 0.025	20.128 ± 0.112	···	19.530 ± 0.117

Table A.2: (continued)

MJD	Epoch (days)	ZTF r (mag)	ZTF g (mag)	ATLAS o (mag)	ATLAS c (mag)
60263.45	17.69	18.772 ± 0.035	···	···	19.543 ± 0.148
60265.49	19.73	···	···	···	19.697 ± 0.140
60266.19	20.43	···	···	18.999 ± 0.115	···
60267.49	21.73	···	···	···	19.979 ± 0.227
60269.51	23.75	···	···	···	19.835 ± 0.173
60281.44	35.68	···	···	19.617 ± 0.187	···
60282.42	36.66	···	···	19.675 ± 0.244	···
60283.41	37.65	···	···	···	20.703 ± 0.330
60284.22	38.46	20.067 ± 0.111	21.329 ± 0.315	19.812 ± 0.116	···
60285.39	39.63	···	···	19.842 ± 0.159	20.322 ± 0.232
60287.37	41.61	···	···	19.544 ± 0.188	20.575 ± 0.222
60288.33	42.57	20.276 ± 0.171	21.000 ± 0.296	20.096 ± 0.217	···
60290.27	44.51	20.273 ± 0.125	20.871 ± 0.178	···	···
60291.42	45.66	···	···	20.104 ± 0.206	···
60292.3	46.54	20.402 ± 0.097	23.062 ± 0.158	19.785 ± 0.172	···
60293.23	47.47	20.569 ± 0.170	22.971 ± 0.296	···	20.461 ± 0.252
60294.22	48.46	20.529 ± 0.118	22.910 ± 0.242	···	···
60295.41	49.65	···	···	20.032 ± 0.201	···
60308.28	62.52	21.533 ± 0.358	···	20.272 ± 0.338	···
60312.36	66.6	···	···	20.427 ± 0.261	···

Table A.3: Expansion velocities and pseudo-equivalent widths.

MJD	Epoch	vCa II IR ($km\,s^{-1}$) (pEW [Å])	vSi II λ5972 ($km\,s^{-1}$) (pEW [Å])	vSi II λ6355 ($km\,s^{-1}$) (pEW [Å])	vO I λ7775 ($km\,s^{-1}$) (pEW [Å])	vCa II H&K ($km\,s^{-1}$) (pEW [Å])	Telescope
60237	−8.66	16114 ± 590	13836 ± 745	14903 ± 334	15035 ± 382	–	UH88
		(285.7 ± 25.3)	(10.2 ± 3.9)	(65 ± 13)	(96.4 ± 30.8)	–	
60240	−5.72	14825 ± 359	11847 ± 181	12639 ± 264	11868 ± 265	16048 ± 341	GTC
		(313.6 ± 5.2)	(50.1 ± 4.1)	(93.9 ± 3.1)	(163.7 ± 4.5)	(91.5 ± 20.4)	
60242	−3.76	14550 ± 441	10760 ± 288	12178 ± 237	11939 ± 102	15592 ± 497	Keck
		(313.9 ± 6.8)	(49.0 ± 2.8)	(111.5 ± 2.2)	(166.7 ± 5.0)	(108.6 ± 5.7)	
60243	−2.78	13431 ± 970	10475 ± 295	11208 ± 284	13404 ± 407	13969 ± 2494	UH88
		(307.3 ± 16.0)	(56.8 ± 7.6)	(111.6 ± 7.1)	(146.0 ± 14.0)	(307.3 ± 16.0)	
60246	0.17	12141 ± 1074	9067 ± 425	10269 ± 498	13244 ± 414	24487 ± 8060	UH88
		(287.3 ± 15.8)	(53.8 ± 14.1)	(116.7 ± 9.4)	(122.9 ± 8.8)	(287.3 ± 15.8)	
60249	3.11	13601 ± 830	8346 ± 187	10717 ± 251	13036 ± 427	16952 ± 772	NOT
		(322.3 ± 10.3)	(45.7 ± 6.2)	(127.5 ± 6.9)	(107.5 ± 10.9)	(216.9 ± 246.6)	
60249	3.11	13732 ± 1135	7894 ± 125	9871 ± 263	11448 ± 99	13803 ± 468	GTC
		(325.6 ± 4.3)	(41.0 ± 2.3)	(141.6 ± 3.8)	(133.4 ± 4.0)	(88.4 ± 14.4)	
60251	5.07	11534 ± 547	7350 ± 410	9999 ± 416	11019 ± 178	32300 ± 6373	UH88
		(321.5 ± 22.7)	(33.1 ± 6.8)	(142.1 ± 9.1)	(102.48 ± 8.0)	(235.2 ± 7.7)	
60251	5.07	–	–	8831 ± 889	11767 ± 760	–	LT
		–	–	(160.5 ± 22.1)	–	–	
60251	5.07	11459 ± 865	6767 ± 385	9736 ± 274	11558 ± 225	44450 ± 974	ESO NTT
		(327.6 ± 46.8)	(35.4 ± 10.7)	(165.6 ± 7.7)	(111.6 ± 13.7)	(268.9 ± 88.9)	
60252	6.05	13155 ± 844	7208 ± 369	9864 ± 332	11019 ± 272	–	UH88
		(335.3 ± 19.9)	(34.1 ± 6.6)	(157.4 ± 10.0)	(96.9 ± 15.1)	–	
60258	11.94	12773 ± 352	–	8735 ± 146	11177 ± 75	10628 ± 583	GTC
		(415.5 ± 2.6)	–	(201.2 ± 4.2)	(87.5 ± 13.7)	(73.0 ± 53.9)	
60264	17.83	12083 ± 615	–	8049 ± 562	10267 ± 708	–	ESO NTT
		(435.8 ± 28.8)	–	(194.4 ± 15.2)	(86.2 ± 21.4)	–	
60265	18.81	9926 ± 1129	–	7976 ± 448	10259 ± 356	11769 ± 536	ESO NTT
		(488.4 ± 17.2)	–	(197.1 ± 8.4)	(63.4 ± 14.2)	(99.4 ± 34.2)	
60267	20.77	12216 ± 276	–	7383 ± 351	11730 ± 81	12316 ± 313	Keck
		(477.7 ± 6.7)	–	(212.6 ± 6.8)	(119.4 ± 6.1)	(94.1 ± 7.8)	
60268	21.75	14173 ± 938	–	7306 ± 419	9801 ± 268	–	UH88
		(468.4 ± 36.6)	–	(205.1 ± 34.1)	(103.4 ± 31.4)	–	
60269	22.73	12709 ± 780	–	7368 ± 198	10726 ± 124	–	Baade
		(477.4 ± 12.7)	–	(219.3 ± 9.7)	(105.9 ± 11.8)	–	
60271	24.7	12705 ± 1250	–	7649 ± 916	9644 ± 529	9209 ± 4453	UH88
		(504.2 ± 29.9)	–	(203.4 ± 48.7)	(96.7 ± 24.5)	–	
60271	24.7	10959 ± 757	–	7312 ± 136	11152 ± 116	11983 ± 269	GTC
		(494.1 ± 6.8)	–	(213.7 ± 6.0)	(121.1 ± 6.4)	(94.9 ± 16.9)	
60284	37.45	10499 ± 732	–	5298 ± 1368	7872 ± 1828	–	UH88
		(523.7 ± 37.4)	–	(177.9 ± 39.8)	(82.1 ± 25.7)	–	
60294	47.26	–	–	1134 ± 2430	33899 ± 1480	11487 ± 771	CAHA
		–	–	(41.4 ± 49.3)	–	(113.6 ± 536.2)	

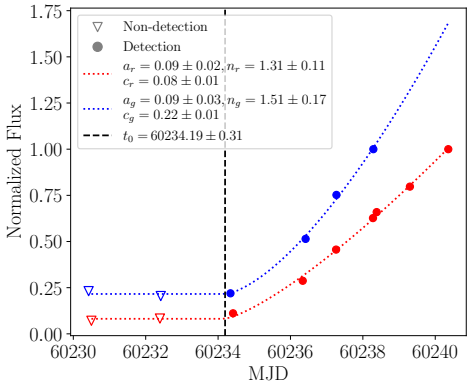


Fig. A.1: Power-law fitting of the early rise of the light curves g, r, $ZTF-g$, $ZTF-r$ of SN 2023vjh. We fit simultaneously the function of eq. 1 for the red and green bands, and we define the explosion date (t_0).

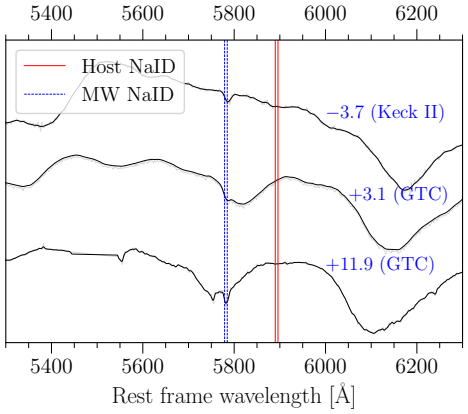


Fig. A.3: Spectra of SN 2023vjh. The position of Na I D absorption lines for Milky Way and the host galaxy are indicated.

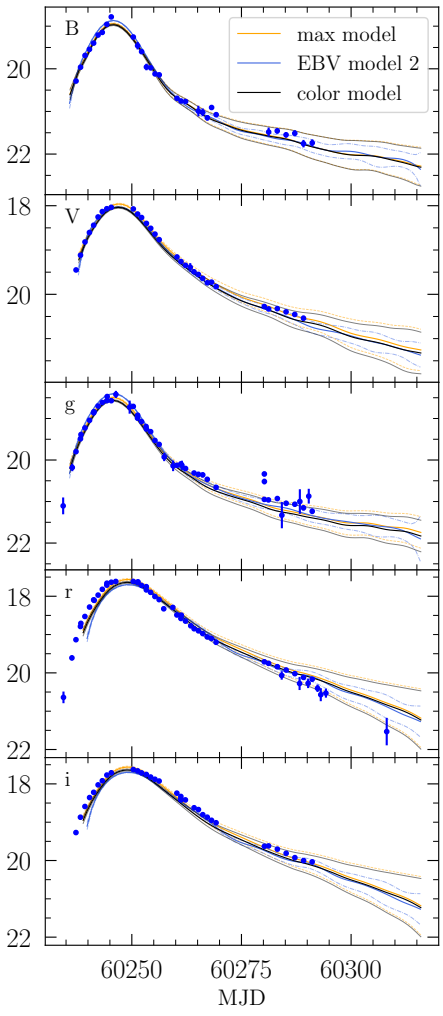


Fig. A.2: Multi-band light curves of `SNooPy` fit of SN 2023vjh using the `max_model` (dashed red line), `EBV_model2` (dash-dotted green line), and `color_model` (dashed black line). All the fits have been done with a 1991bg-like template.

Table A.4: Spectroscopic log.

UT date	MJD	Epoch	Telescope	Range/Grism
2023-10-20	60237	−8.7	UH88	3000 - 10000
2023-10-23	60240	−5.8	GTC	R1000B/R1000R
2023-10-25	60242	−3.8	Keck II	3000 - 10000
2023-10-26	60243	−2.8	UH88	3000 - 10000
2023-10-29	60246	+0.1	UH88	3000 - 10000
2023-11-01	60252	+3.1	GTC	R1000B/R1000R
2023-11-01	60249	+3.1	NOT 2.6m	gr4
2023-11-03	60251	+5.0	UH88	3000 - 10000
2023-11-03	60251	+5.0	LT	blue
2023-11-03	60251	+5.0	ESO NTT	gr11+gr16
2023-11-04	60252	+6.0	UH88	3000 - 10000
2023-11-10	60258	+11.9	GTC	R1000B/R1000R
2023-11-16	60264	+17.8	ESO NTT	gr13
2023-11-17	60265	+18.8	ESO NTT	gr16
2023-11-19	60267	+20.7	Keck II	3000 - 10000
2023-11-20	60268	+21.7	UH88	3000 - 10000
2023-11-21	60269	+22.7	Baade	4230 - 9418
2023-11-23	60271	+24.7	UH88	3000 - 10000
2023-11-23	60271	+24.7	GTC	R1000B/R1000R
2023-12-06	60284	+37.4	UH88	3000 - 10000
2023-12-15	60294	+47.2	CAHA Tel. 3.5m	V500 - IFU

Appendix B: Position of SN 2023vjh in classification diagrams

In previous surveys, the spectroscopic properties of SNe Ia near maximum light have been used to classify them into different subtypes and to identify peculiar or uncommon events (e.g. Branch et al. 2006; Blondin et al. 2012; Folatelli et al. 2013; Morrell et al. 2024). Here, we reproduce some of these classification diagrams in order to examine the position of SN 2023vjh within this context. Based on these earlier works, 91bg-like SNe Ia are expected to fall within the region occupied by "cool" SNe Ia, which are characterised by lower photospheric temperatures and spectra dominated by strong low-ionisation features such as Fe II, Ti II, and Ca II (Nugent et al. 1995; Mazzali et al. 1997; Branch et al. 2006).

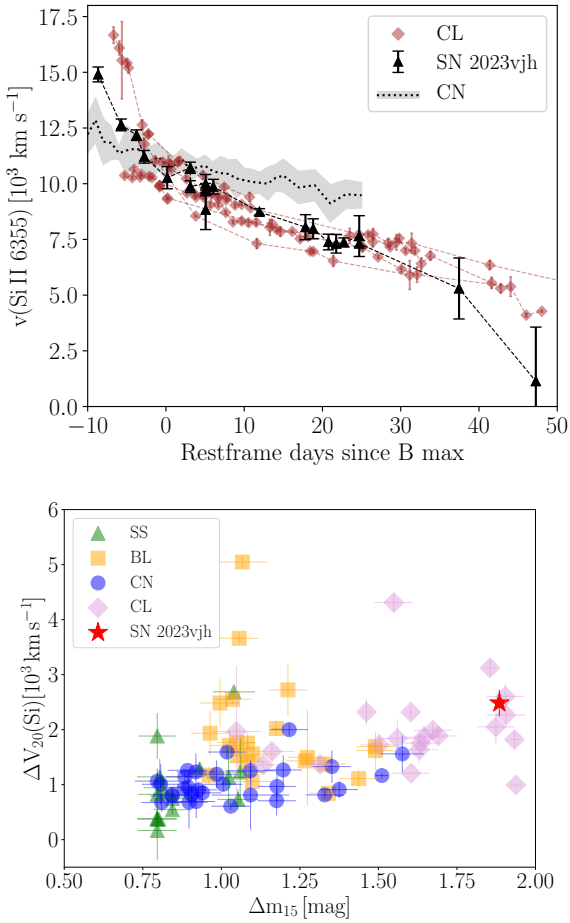


Fig. B.1: *Upper panel:* Si II λ6355 expansion velocity of SN 2023vjh (black triangles) and other cool (CL) SNe. The black-dotted line indicates the mean Si II λ6355 velocity of core normal (CN) SNe and the grey zone its uncertainty (Morrell et al. 2024). *Lower panel:* Si II λ6355 velocity decline rate as a function of the Δm_{15}. The red star indicates the position of SN 2023vjh, while the rest of the sources have been obtained by Morrell et al. (2024).

In Fig. B.1 (upper panel) we show the temporal evolution of the Si II λ6355 expansion velocity for SN 2023vjh (black line), alongside the sample of cool SNe from Folatelli et al. (2013). The Si II λ6355 velocity in SN 2023vjh follows the same decline trend as the cool SNe Ia (shown in brown), which typically exhibit faster velocity decreases than core-normal SNe Ia, particularly after *B*-band maximum. For comparison, we also include the mean Si II λ6355 velocity evolution and its uncertainties for core-normal SNe from Morrell et al. (2024), highlighting the clear difference between the two populations.

Agreement of SN 2023vjh with other cool SNe Ia is also seen in Fig. B.1 (lower panel), where we show the difference in the expansion velocity of Si II λ6355 between maximum light and 20 days after B-band maximum, as a function of Δm_{15} for the sample of CSP-I, CSP-II, and historical SNe Ia (Morrell et al. 2024). The different classes of SNe Ia presented in this diagram are core normal (CN), cool (CL), shallow silicon (SS), and broad lined (BL). SN 2023vjh is located in the region of cool SNe Ia, which occupies the rightmost part of the plot.

In Fig. B.2, we show on the left the Branch et al. (2006) diagram and on the right the Wang et al. (2009) diagram, where different subcategories of SNe Ia are distinguished. For the Branch diagram we used the code developed by Burrow et al. (2020), formulated to determine group membership probabilistically. Different colours and shapes correspond to different classes (CN, SS, BL, CL) of SNe from the CSP-I+II (Folatelli et al. 2013; Krisciunas et al. 2017; Hsiao et al. 2019; Phillips et al. 2019; Morrell et al. 2024), while the SNe 2023vjh, 1991bg, 1999by, 2002es, 2005bl, 2005ke, 2006mr, and 2022xkq (Pearson et al. 2024) have been included indicated by a number. In both cases, SN 2023vjh occupies the region associated with CL SNe. In the Branch diagram, it lies well within the cool region, where 91bg-like SNe Ia are typically found. In the Wang et al. (2009) diagram, it is located closer to the area that overlaps with the core-normal SNe Ia. Figure B.3 (a) shows the *pEW* width of Si II λ5972 versus s_{BV}, for the CSP-I+II, and historical SN Ia samples (Morrell et al. 2024). SN 2023vjh is located in the rightest portion of the locus of cool SNe.

Additionally, we examined whether SN 2023vjh falls into the 'extremely cool' (eCL) sub-class as defined by Folatelli et al. (2013). Cool SNe are characterised by strong absorption around 4300 Å, primarily due to prominent Ti II features. According to Folatelli et al. (2013), eCL SNe are those with $pEW > 220$ Å near maximum light (they call it $pEW_{\rm Mg\,II}$, but here we use the name $pEW_{\rm Ti\,II}$), and they typically show a weighted-average $pEW_{\rm Ca\,II\,IR}$ of 325 ± 39 Å. We measured these *pEW*s for SN 2023vjh around maximum (using the weighted mean over ± 5 days) and obtained $pEW_{\rm Ti\,II} = 292.5 \pm 8.3$ and $pEW_{\rm Ca\,II\,IR} = 320.2 \pm 3.2$. Based on the Ti II criterion, SN 2023vjh therefore qualifies as an eCL SN, placing it in the same group as SN 2005bl, SN 2005ke, SN 2006bd, SN 2006mr, SN 2007ax, and SN 2009F reported in Folatelli et al. (2013). Finally, in Fig. B.3 (b), using the *pEW* of the absorption feature at 4000 Å, we examined where SN 2023vjh is located in the pEW(4000 Å)–s_{BV} diagram, in comparison with different SN groups (Alburai et al. 2026). SN 2023vjh occupies the upper region of the 91bg-like SNe.

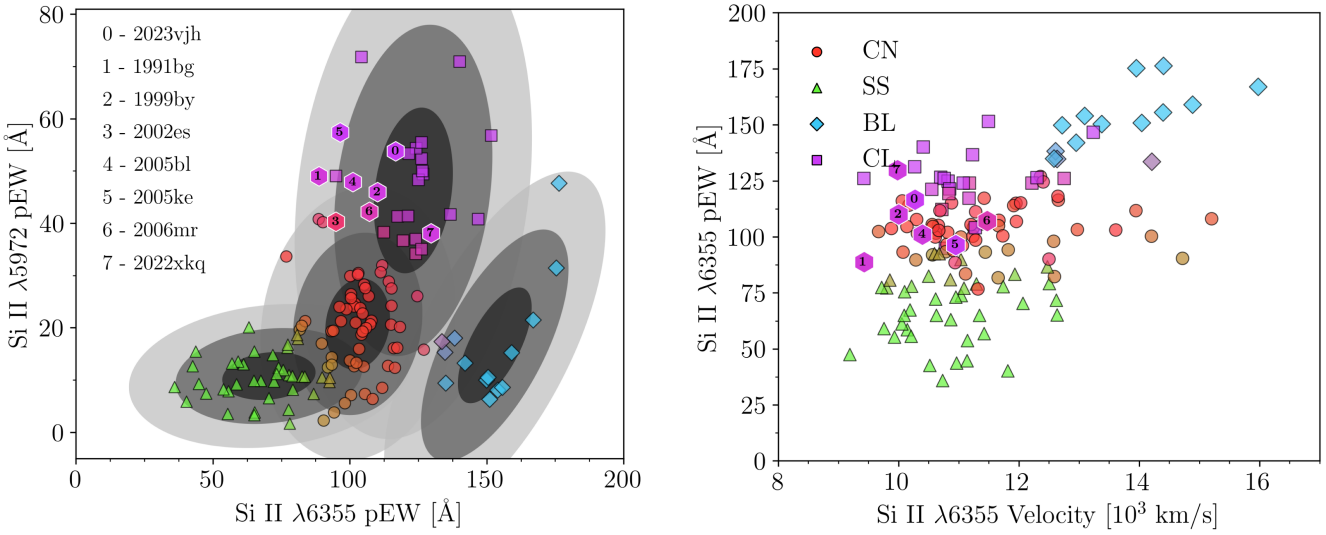


Fig. B.2: Branch et al. (2006) and Wang et al. (2009) diagrams (left and right panels respectively). For the Branch diagram we used the code developed by Burrow et al. (2020), formulated to determine group membership probabilistically. Different colours and shapes correspond to different classes (CN, SS, BL, CL) of SNe from the CSP-I+II (Folatelli et al. 2013; Krisciunas et al. 2017; Hsiao et al. 2019; Phillips et al. 2019; Morrell et al. 2024). In both cases SN 2023vjh is marked with the number zero. For SN 2023vjh the $pEW_{\mathrm{Si\,II\,6355}} = 116.7 \pm 9.4$ Å, $pEW_{\mathrm{Si\,II\,5972}} = 53.8 \pm 14.1$ Å, and $v_{\mathrm{Si\,II\,6355}} = 10269 \pm 498\,\mathrm{km\,s^{-1}}$.

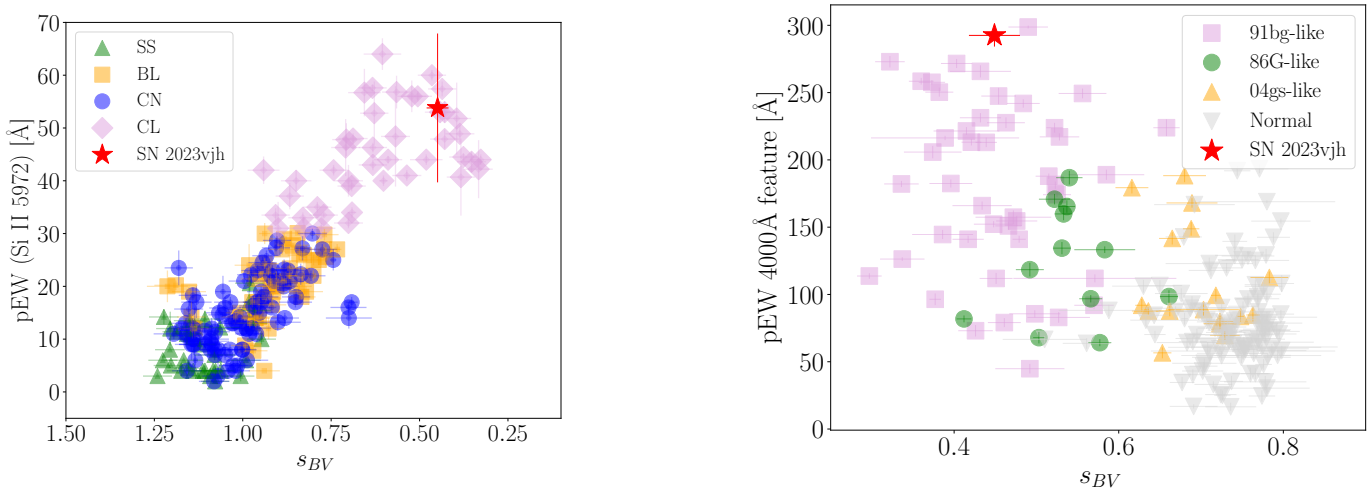


Fig. B.3: *Left:* pEW of Si II λ5972 as a function of s_{BV}. The red star indicates the position of SN 2023vjh. The rest of the sources have been obtained from Morrell et al. (2024); *Right:* A pEW diagram of the 4000Å feature as a function of s_{BV}, for four SNe Ia groups, as presented in Alburai et al. (2026).